Spring 1-1-2014

Use of DNS Data for the Evaluation of Closure Models in Spanwise-Rotating Turbulent Channel Flow

Alan Sean-Ker Hsieh
University of Colorado Boulder, alan.hsieh@colorado.edu

Use of DNS Data for the Evaluation of Closure Models in Spanwise-Rotating Turbulent Channel Flow

by

Alan Hsieh

B.S., University of Southern California, 2011

A thesis submitted to the

Faculty of the Graduate School of the

University of Colorado in partial fulfillment

of the requirements for the degree of

Master of Science

Department of Aerospace Engineering Sciences

2014

This thesis entitled:
Use of DNS Data for the Evaluation of Closure Models in Spanwise-Rotating Turbulent Channel Flow
written by Alan Hsieh
has been approved for the Department of Aerospace Engineering Sciences

_____
Sedat Biringen

_____
Professor John Evans

_____
Professor Mahmoud Hussein

Date _____

The final copy of this thesis has been examined by the signatories, and we find that both the content and the form meet acceptable presentation standards of scholarly work in the above mentioned discipline.

Hsieh, Alan (M.S., Aerospace Engineering Sciences)

Use of DNS Data for the Evaluation of Closure Models in Spanwise-Rotating Turbulent Channel Flow

Thesis directed by Professor Sedat Biringen

A direct numerical simulation (DNS) of a spanwise-rotating turbulent channel flow was conducted for three rotation numbers: $Ro_c = 0$, 5.2 and 26, at a Reynolds number $Re_c = 8000$. The data base obtained from these simulations was used to evaluate several commonly used Reynolds-Averaged Navier-Stokes (RANS-based) closure models for rotating turbulent channel flows. It was shown that the Reynolds stresses predicted by the Speziale-Gatski (SG) model were the most consistent with the DNS results. A correction to the Girimaji turbulence model was proposed to remove a discontinuity in the non-rotational case. The pressure-strain functions of the explicit algebraic Reynolds stress model (EARSM)-type SG and Girimaji models were examined and the modeled pressure-strain distributions of both turbulence models, especially near the suction wall, were demonstrated to become more accurate with increasing rotation number. The accuracy of the modeled pressure-strain was also shown to affect the accuracy of the corresponding modeled Reynolds stresses near the channel walls.

Dedication

Dedicated to my family, friends and mentors who have supported me throughout my path in education.

Acknowledgements

First and foremost, I would like to thank Professor Biringen for all of his great support and advice throughout my graduate study. The quality of my research and this thesis would not have been possible without the insightful input and great guidance given to me by my research advisor. I would also like to thank my colleague Alec Kucala for his ever-present availabiity to answer questions and his mentoring and tutelage especially in the field of computation, and Scott Waggy for allowing me to use his atmospheric boundary layer code as the basis of my present direct numerical simulation code. I would also like to thank the National Institute of Computational Sciences and the Texas Advanced Computing Center for providing the necessary computational resources for my research. And finally, thanks to the University of Colorado's Department of Aerospace Engineering Sciences for providing me the necessary financial support over the course of my graduate studies.

Contents

Tables

Table

Figures

Figure

Chapter 1

Introduction

When a turbulent channel flow is subject to rotation in the spanwise direction, asymmetry is observed across the channel and is distinguished by reduced turbulence levels near one wall and elevated turbulence levels near the opposite wall; these regions are known as the suction and pressure sides, respectively (Grundestam, Wallin, and Johansson, 2008). Subsequently, the symmetric profiles of Reynolds-stresses, mean velocity, and velocity fluctuations in a non-rotating channel become asymmetric with respect to the channel center-line as a result of rotation. The effects of spanwise rotation on the momentum characteristics of turbulent channel flow have been well documented in previous direct numerical simulation (DNS) studies by Grundestam et al. (2008) and Wu and Kasagi (2004).

Turbulence is already a complex scientific field due to the chaotic and unpredictable nature of turbulent flows and structures, and the rotation-induced additional body forces (Coriolis, centrifugal) only cause momentum transport mechanisms to become more complicated. Turbulent flows, not laminar flows, are predominantly found in nature, and with the prevalence of rotation-dependent machinery in engineering, a physical understanding of turbulent flow in rotating systems is prudent for engineering and scientific analyses. Hence, research into this type of flow has relevance to practical engineering applications such as turbine blades and rotating turbomachinery design especially with regards to surface heat transfer and skin friction.

In order to assess the effects of spanwise rotation on the momentum balance in turbulent channel flow within this work, a direct numerical simulation was employed to integrate the time-

dependent, three-dimensional Navier-Stokes equations. The resulting DNS data base was then used to test the accuracy of three commonly-cited Reynolds-Averaged Navier-Stokes (RANS) closure models, the $\overline{v^2} - f$, Speziale-Gatski (SG) and Girimaji models, proposed by Reif, Durbin, and Ooi (1999), Speziale and Gatski (1993), and Girimaji (1996), respectively, in modeling Reynolds stresses for spanwise-rotating turbulent channel flow.

Computational modeling of all types of turbulent flows has been essential to the field of engineering since the advent of the computer, allowing for engineering analysis to extend beyond theory and physical experimentation. As computers have increased in complexity and computational power in the recent decades, three main forms of computational methods for turbulence modeling have arisen. Direct numerical simulation (DNS) is a computational simulation in which the three-dimensional, time-dependent Navier-Stokes equations are numerically solved along with the full range of spatial and temporal scales of turbulence, resulting in the most accurate computational solutions. However, direct numerical simulations are frequently cost-prohibitive due to the high computational cost of resolving all scales, especially in cases of complex geometry and flow configurations. Large eddy simulation (LES) is another computational simulation that solves the three-dimensional, time-dependent Navier-Stokes equations similar to DNS, but only for large-scale turbulence. For the smallest scales of turbulence such as the Kolmogorov microscales, model functions known as subgrid-scale models are used to approximate the contributions from these smaller scales into the rest of the LES (Reynolds, 1976). The flexibility of LES in choosing the size of the filter separating the large and small scales allows for model adaptation to available computational resources, although LES has decreased accuracy compared to DNS as some scales of turbulence are not fully resolved, only modeled.

The third type of computational modeling is known as Reynolds-Averaged Navier-Stokes (RANS) based modeling. In RANS modeling, there is no numerical solution of the Navier-Stokes equations such as in DNS and LES, instead an alternative form of the Navier-Stokes equations known the Reynolds stress equation is derived and partial differential equations of various flow quantities within this equation are solved for (Reynolds, 1976). While RANS-based models are

the least accurate of the three main computational models, these models are also require far less computational power and therefore a RANS-based model that can model turbulence in flow fields with accuracy similar to DNS or LES is very desirable in the engineering field. There are many levels of RANS-based models: the simplest levels include zero-equation, one-equation, and two-equation models, which solve a pde related to the mean velocity field, a pde related to a turbulent velocity scale, and two pdes related to both a turbulent velocity and length scale, respectively (Reynolds, 1976). However, these simpler RANS-based models are generally unable to properly model rotational flows and are subsequently disregarded in this work. For flows involving rotation, nonlinear eddy viscosity models are the most frequently applied RANS-based models, which include the two model subtypes $\overline{v^2} - f$ models and explicit algebraic Reynolds stress models, both of which are considered in this work. For a suitable data base to compare and test these RANS-based models, a more accurate computational solution was required; due to the relatively simple geometry of rotating turbulence channel flow, a direct numerical simulation was conducted for this study instead of a large eddy simulation.

Other variations of computational modeling also exist. For example, detached eddy simulation (DES) is a combination of RANS modeling and LES where subgrid-scale models are used to model flow regions where the turbulent length scale exceeds the grid dimensions and the RANS method is used to solve the flow regions where the turbulent length scale is less than the maximum grid dimension (generally in the near-wall region). Coherent vortex simulation is another computational approach in which the turbulent flow field is decomposed into coherent and non-coherent sections using wavelet filtering; the coherent section is then resolved in a similar method to LES. Unsteady Reynolds-Averaged Navier-Stokes (URANS) models, partially integrated transport models (PITM), and hybrid LES-RANS (HLS) models are additional computational methods that are mixtures of LES and RANS to varying degrees.

Of the three major flow simulation methods: DNS, LES and RANS modeling, RANS-based turbulence models are the most practical as they offer the lowest computational cost. The three aforementioned turbulence models, which are of the most common RANS-based model type used

to model rotational flows, are all nonlinear eddy viscosity models. These RANS-based models produce model closure for the Reynolds stress equation by solving partial differential equations of important flow quantities, such as the turbulent kinetic energy k and the turbulent energy dissipation rate ε. Both the SG and Girimaji models, explicit algebraic Reynolds stress models (EARSM), additionally construct an implicit model for the anisotropic tensor b_{ij} from the partial differential equations of the energy budget terms in the Reynolds stress equation, and then derive an explicit form for b_{ij} analytically. The effect of the anisotropic tensor is seen in the pressure-strain function proposed by Speziale, Sarkar, and Gatski (1991) (SSG) that is present in both of these models, and the modeled pressure-strain values of these two models are directly compared to the pressure-strain values extracted from the DNS. Previous research has shown that the pressure-strain correlation term exerts a powerful influence on many turbulent quantities such as the turbulent kinetic energy (Launder, Reece, and Rodi, 1975), and hence we also investigate these two EARSM-type models in regards to correlating the accuracy of the modeled pressure-strain with the accuracy of the modeled Reynolds-stresses for the SG and Girimaji turbulence models.

This paper is organized as follows: the second section will cover the numerical method, parameters and specifications used in the direct numerical simulation and the DNS validation. The third section will provide an overview of the three RANS-based turbulence models considered in this work and a comparison of the modeled Reynolds stresses with the DNS; a correction to the Girimaji model for the non-rotational case is also proposed in this section. The final section will analyze the accuracy of the SG and Girimaji pressure-strain functions and draw correlations between the modeled pressure-strain and modeled Reynolds stresses for the two turbulence models.

Chapter 2

Numerical Method and Case Descriptions

The time-dependent, three-dimensional incompressible Navier-Stokes equations were integrated in a doubly periodic (in x and z-directions) turbulent channel flow using a fractional step method (Waggy, Biringen, and Sullivan, 2013). With all spatial coordinates non-dimensionalized by the channel half-height δ and velocities by the centerline velocity U_c, the Navier-Stokes equations read (in conservative form)

$$\frac{\partial u_i}{\partial x_i} = 0 \tag{2.1}$$

$$\frac{\partial u_i}{\partial t} + \frac{\partial u_i u_j}{\partial x_j} = -\frac{\partial p}{\partial x_i} + \frac{1}{Re_c}\frac{\partial^2 u_i}{\partial x_i \partial x_j} - Ro_c \varepsilon_{ijk}\frac{\Omega_j}{\Omega}u_k \tag{2.2}$$

where $Re_c = U_c\delta/\nu$, ν is the kinematic viscosity, and the vector $\mathbf{u} = \langle u, v, w \rangle$ is composed of three velocity components in the x (streamwise), y (wall-normal), and z (spanwise) directions, respectively. Also, p represents non-dimensionalized pressure and t represents non-dimensionalized time. The rotation number, or Rossby number, is defined as $Ro_c = 2\Omega\delta/U_c$ where Ω is the spanwise angular rotation vector.

The flow geometry is shown in figure 2.1, and the flow field is assumed to be statistically homogeneous in the streamwise (x) and spanwise (z) directions. Hence, periodic boundary conditions are applied in both of those directions. Due to turbulent channel flow being a wall-bounded flow, velocity boundary conditions at the walls ($y = 0$, 2) were assumed to be no-slip.

Figure 2.1: Diagram of turbulent channel flow with rotation in the spanwise direction.

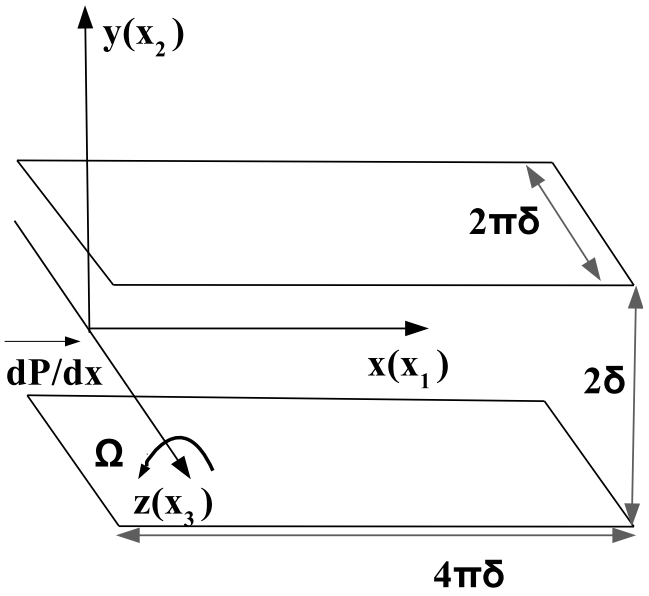

2.1 Time Integration Scheme

All of the numerical methods and schemes presented in this work were performed using a Navier-Stokes solver developed by Waggy (2009) for the simulation of the turbulent Ekman layer. This code was further modified for plane channel flow (Kucala and Biringen, in press.) and periodic channel flow; rotational effects were added and implemented smoothly in the present work. The time integration scheme used is the semi-implicit Adams-Bashforth/Crank-Nicolson (ABCN) method, which makes the numerical procedure second order accurate in time (Waggy et al., 2013). The Crank-Nicholson method uses an implicit scheme for the diffusion terms in equation 2.2, which is written as

$$\frac{\hat{u}_i - u_i^n}{\Delta t} \approx \frac{1}{2\mathrm{Re}}\frac{\partial^2 \hat{u}_i}{\partial x_3^2} + \frac{1}{2\mathrm{Re}}\frac{\partial^2 u_i^n}{\partial x_3^2} + \mathcal{O}\left(\Delta t^2\right) \tag{2.3}$$

where the predicted velocity $\hat{u}_i$ is solved implicitly using the linear system of equations shown in equation 2.4.

$$\left(1 - \frac{\Delta t}{2\mathrm{Re}}\frac{\partial^2}{\partial x_3^2}\right)\hat{u}_i \approx u_i^n + \frac{\Delta t}{2}M_i^n \tag{2.4}$$

with

$$M_i^n = \frac{1}{\mathrm{Re}}\frac{\partial^2 u_i^n}{\partial x_3^2} \tag{2.5}$$

The remaining terms in equation 2.2 are solved using the explicit Adams-Bashforth scheme as shown in equation 2.6,

$$\frac{\hat{u}_i - u_i^n}{\Delta t} \approx \frac{3}{2}L_i^n - \frac{1}{2}L_i^{n-1} + \mathcal{O}\left(\Delta t^2\right) \tag{2.6}$$

where

$$L_i^n = -\frac{\partial u_i^n u_j^n}{\partial x_j} - \frac{1}{\mathrm{Ro}}u_j^n \varepsilon_{ji3} - \frac{\partial P}{\partial x_i} + \frac{1}{\mathrm{Re}}\left(\frac{\partial^2 u_i^n}{\partial x_1^2} + \frac{\partial^2 u_i^n}{\partial x_2^2}\right) \tag{2.7}$$

Combining both expressions from the Adams-Bashforth and Crank-Nicholson schemes yields the expression for the predicted velocity in equation 2.8.

$$\left(1 - \frac{\Delta t}{2\mathrm{Re}}\frac{\partial^2}{\partial x_3^2}\right)\hat{u}_i = u_i^n + \Delta t\left(\frac{1}{2}M_i^n + \frac{3}{2}L_i^n - \frac{1}{2}L_i^{n-1}\right) \tag{2.8}$$

Once the predicted velocity $\hat{u}_i$ is computed, the velocity at the next time step $(n+1)$ is found by applying a corrector step as shown in equation 2.9, with ϕ representing the pseudo-pressure.

$$u_i^{n+1} = \hat{u}_i - \Delta t \frac{\partial \phi}{\partial x_i} \tag{2.9}$$

The pseudo-pressure is computed by taking the divergence of equation 2.9 and enforcing equation 2.1 (continuity) at the next time step, yielding the expression shown in equation 2.10.

$$-\Delta t \frac{\partial^2 \phi}{\partial x_i \partial x_i} = \frac{\partial \hat{u}_i}{\partial x_i} \tag{2.10}$$

2.2 Spatial Differences

The spatial derivatives are computed using a finite-difference approximation in all coordinate directions with fourth order central differences by means of high-order Lagrangian polynomials. The streamwise (u) and spanwise (w) velocity components are discretized on a "centered" vertical mesh, while the wall-normal (v) velocity component is discretized on a "staggered" vertical mesh to enhance coupling between the vertical velocity and the pressure (Waggy et al., 2013).

In order to dissipate excess energy that remains unsolved by the grid when applying finite difference methods, an artificial viscosity in physical space must be implemented to ensure numerical smoothing and account for dealiasing. In this numerical integration scheme, this is applied by adding a high-order dissipation term to the finite difference equations as shown in equation 2.11; the dissipation term β was set to a value of 0.15.

$$L_i^n = \cdots + \beta \Delta x_j^4 \frac{\partial^4 u_i^n}{\partial x_j^4} \tag{2.11}$$

2.3 Case Parameters and Descriptions

The Reynolds number based on the laminar centerline velocity $Re_c = 8{,}000$ was kept constant for the present simulations; the friction Reynolds number Re_τ was allowed to vary. The grid resolution used was $256 \times 129 \times 256$ in the streamwise (x), wall-normal (y), and spanwise (z) directions, respectively. The domain lengths were selected as $L_x = 4\pi\delta$, $L_y = 2\delta$, and $L_z = 2\pi\delta$ for

Table 2.1: Case Descriptions and Initial Conditions

Case	Re_m	Re_τ	Ro_m	Ro_τ	$\frac{u_c}{u_\tau}$
A	2966	184	0	0	18.6
B	3018	182	0.10	1.7	18.9
C	3106	174	0.50	8.8	21.1

all simulations to adequately fit the largest scales of motion. A summary of the different cases is found in table 2.1. Quantities denoted by subscripts of m, c, and τ correspond to scaling using the mean bulk velocity, mean channel center-line velocity, and global friction velocity, respectively. For all cases, the Navier-Stokes equations were integrated until a quasi-periodic steady-state was reached and each successive case with increasing rotation number was initiated using the steady-state data base attained by the previous case. The original data base for the non-rotating case (A) was initialized from an non-converged data field of non-rotating turbulent channel flow given to this work's author by colleague Alec Kucala.

The numerical procedure outlined in the previous section was programmed using the Portable, Extensible Toolkit for Scientific Computation (PETSc). As PETSc routines are designed for solving massive systems of equations, implementation of the PETSc libraries enabled the simulation code to run optimally using as few processors as possible. As linear solvers are necessary to compute the pseudo-pressure and predicted velocity, all solutions were obtained using Krylov subspace methods found within the routines of the PETSc library; the convergence tolerance of the linear systems was $1e^{-7}$. Simulations were run on the Kraken Cray XT5 system located at the National Institute for Computational Sciences for a total run time of over 1000 nondimensional time units. The value of the time step was 0.002 for all simulations and was chosen to optimize the flow field convergence time while ensuring numerical stability; the total number of iterations exceeded half a million.

The quasi-periodic steady-state for all simulation cases was characterized by two requirements: a convergence of the normal and shear Reynolds stress profiles and a sufficient leveling

of the turbulent Reynolds number over a nondimensional time period of $T = 20$. This second requirement was established due to a consistent decrease of the turbulent Reynolds number over time after an initial increase in value from the added rotation, and to ensure a large enough sample size so that a satisfactory data base for time-averaging could be collected. The distribution of the friction Reynolds number Re_τ over nondimensional time T for simulation cases A, B and C are shown in figures 2.2, 2.3 and 2.4, respectively; these figures also display the time spans over which the time-averaged data used for the present DNS profile distributions was collected.

Figure 2.2: Re_τ ($Ro_m = 0$). - - -: Distribution over time. —: Time span used for time-averaged data.

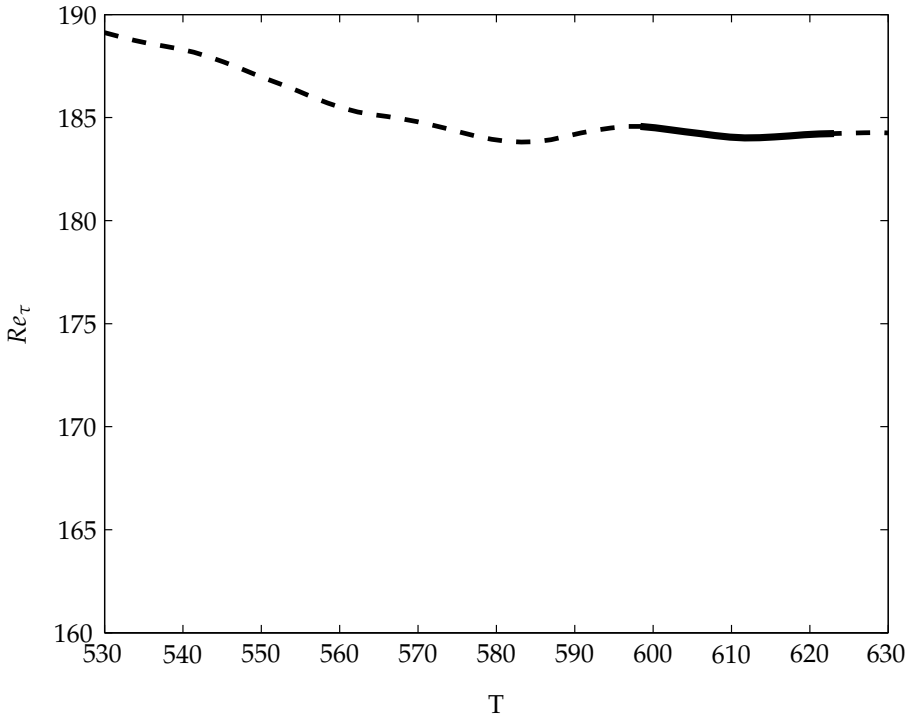

Figure 2.3: Re_τ ($Ro_m = 0.1$). - - -: Distribution over time. —: Time span used for time-averaged data.

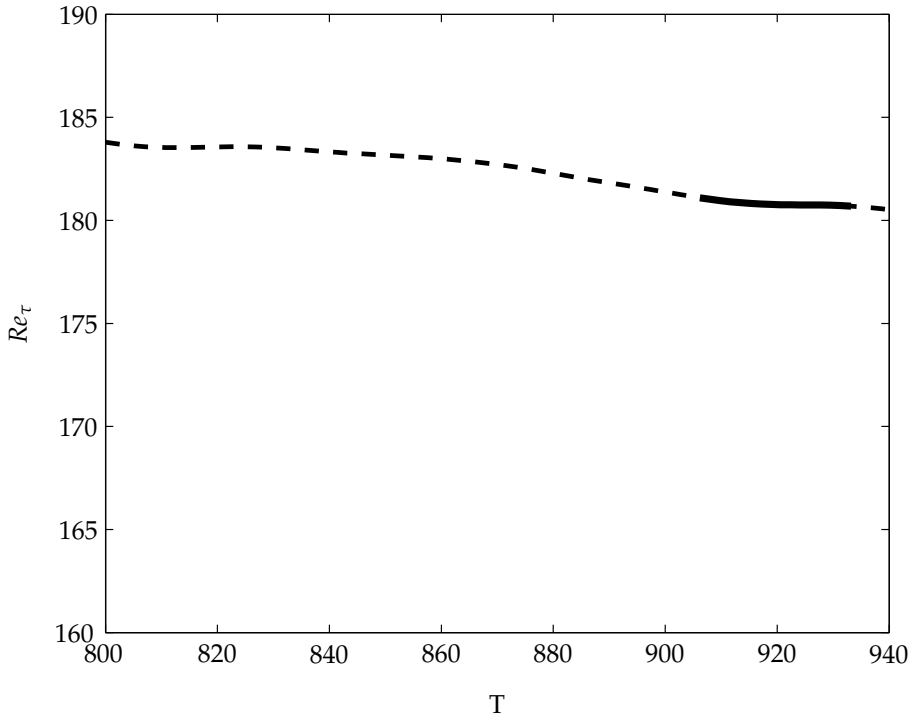

Figure 2.4: Re_τ ($Ro_m = 0.5$). - - -: Distribution over time. —: Time span used for time-averaged data.

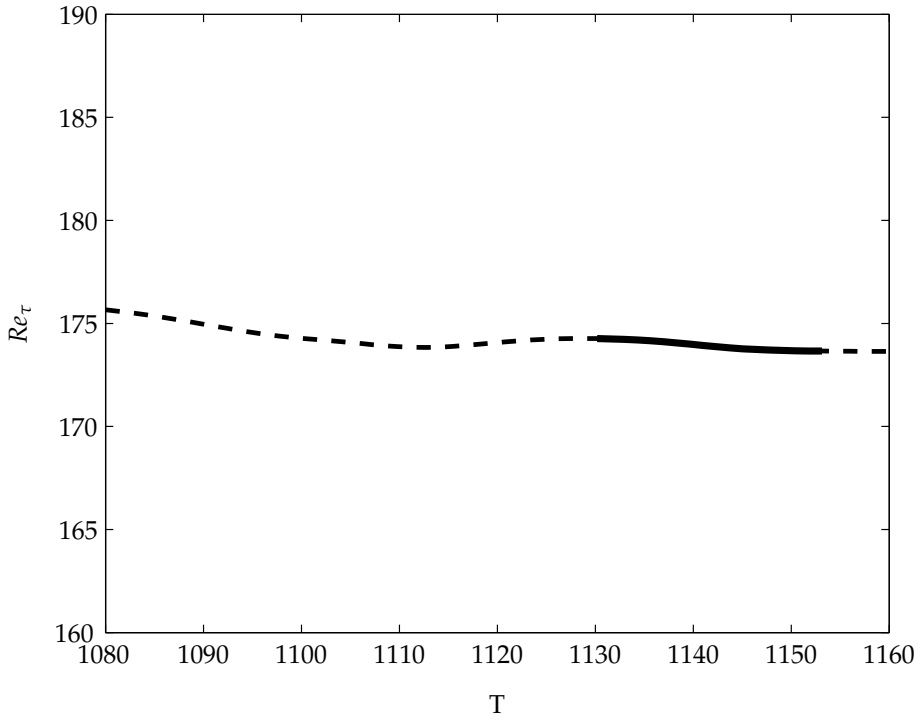

As the streamwise and spanwise directions are assumed periodic and therefore infinite, all profiles were averaged along those directions. For all cases, the momentum statistics were time-averaged and denoted by an overbar $\overline{()}$ for a dimensionless time period of 20 with a hundred evenly-spaced samples. These quantities were then scaled by the global friction velocity u_τ.

2.4 Present Direct Numerical Simulation Results

2.4.1 Total shear stress, law of the wall, energy spectra and mean velocity

For the nonrotating case (A), the total "kinematic" shear stress is shown along with the primary Reynolds shear stress $\overline{u'v'}$ in figure 2.5. The profile of the total shear stress is linear in the case of fully developed channel flow (Kim et al., 1987), and the computed result shows agreement. Additionally, the law of the wall is plotted for the non-rotating case (A) along with the accepted approximations for the viscous sublayer and log-law regions in figure 2.6. The Von Karman con-

stant κ and constant C have the values 0.41 and 5.8, respectively, and the normalized velocity distribution displays the appropriate profiles in the viscous sublayer and log-law regions. To show the adequacy of the grid resolutions and computational domain for high wavenumbers, the energy spectra in the streamwise (x) and spanwise (z) directions are shown in figure 2.7 at selected points near the center-line and channel wall. The results demonstrate that the energy density corresponding to high wavenumbers is several orders of magnitude smaller than the energy density associated with low wavenumbers and that there is no evidence of aliasing at high wavenumbers at this grid resolution.

Figure 2.5: Distribution of the shear stresses. —: $-\overline{u'v'}$. - - -: $-\overline{u'v'} + Re_\tau dU/dy$

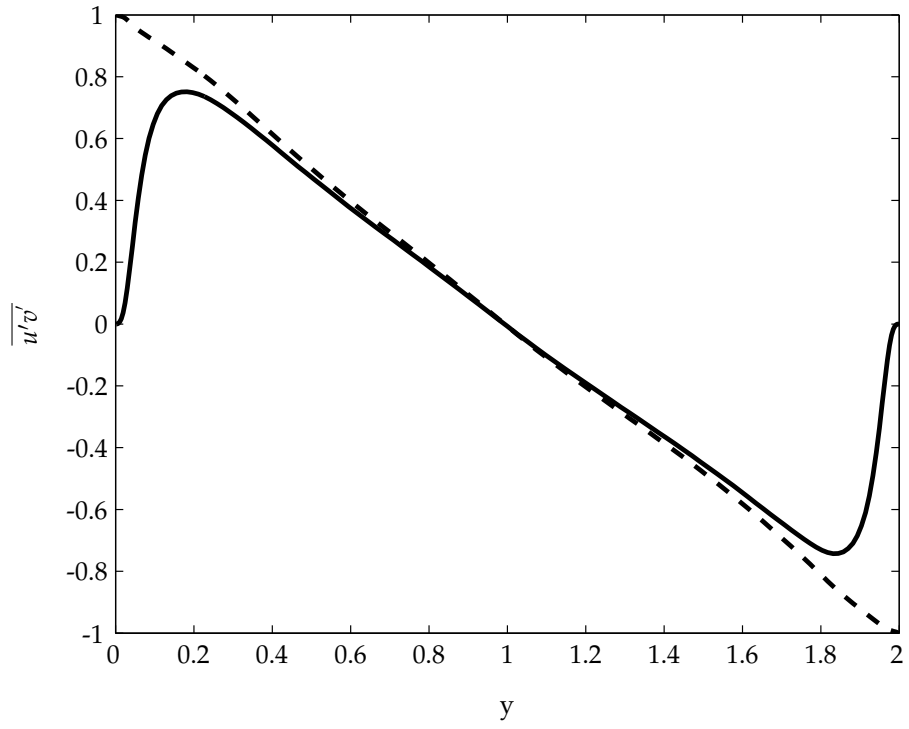

Figure 2.6: Law of the wall. —: DNS velocity distribution; - - -: $U^+ = y^+$; - ·: $U^+ = \frac{1}{\kappa} ln(y^+) + C$

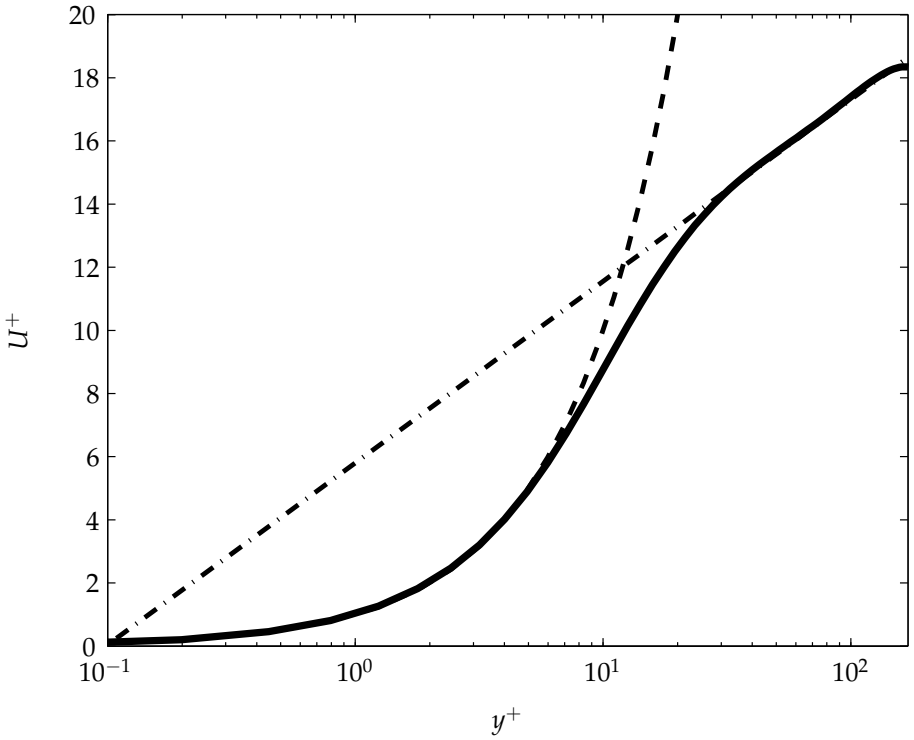

Figure 2.7: One-dimensional energy spectra: (a) Streamwise ($\frac{y}{\delta} = 0.03$); (b) Spanwise ($\frac{y}{\delta} = 0.03$); (c) Streamwise ($\frac{y}{\delta} = 0.85$); (d) (b) Spanwise ($\frac{y}{\delta} = 0.85$);

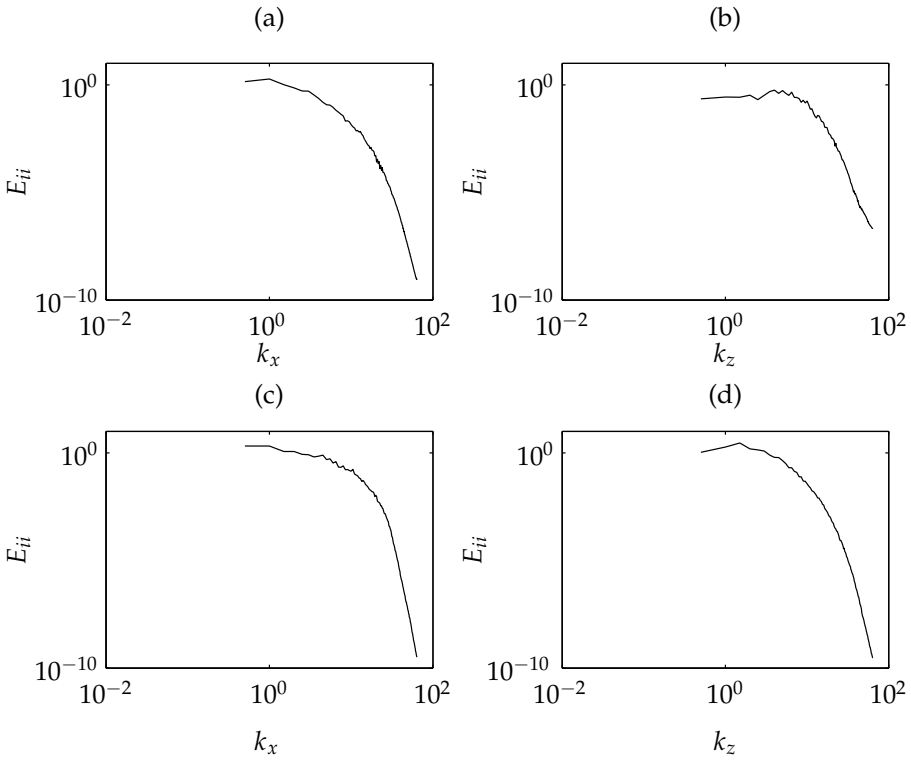

Figure 2.8: Mean velocity profiles. —: Case A; - - -: Case B; · · ·: Case C, - ·: 2Ω lines

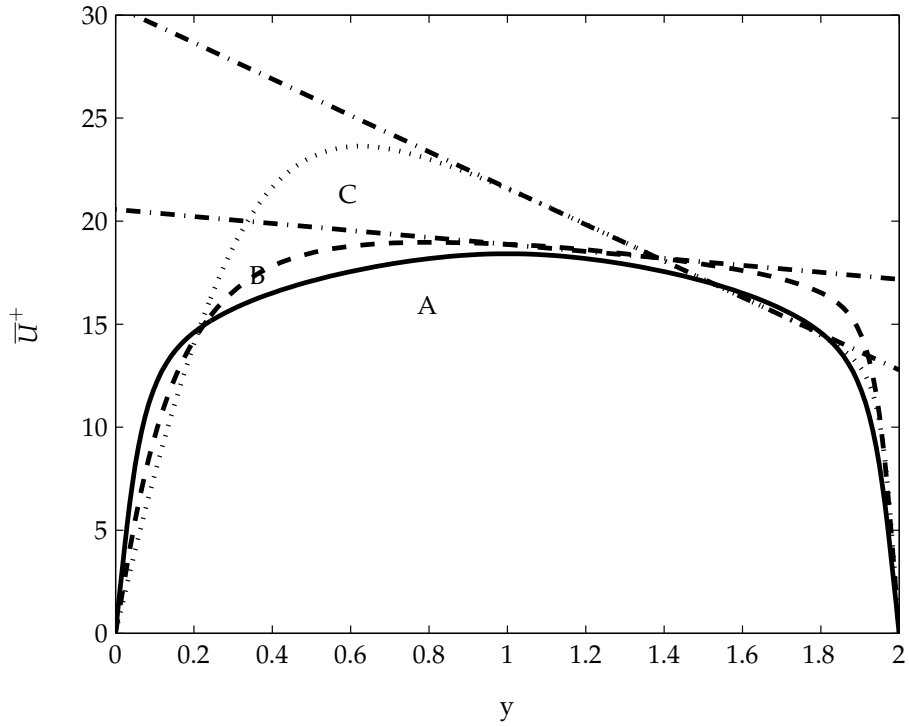

The expected asymmetric stratification of the mean velocity profiles subjected to spanwise rotation (cases $B - C$) is shown in figure 2.8. As observed experimentally and computationally by Johnston, Halleen, and Lezius (1972) and Kristofferson and Andersson (1993), respectively, a region in the channel where the mean velocity varies linearly across the channel walls is created as a result of the spanwise rotation and is characterized by a linear slope of -2Ω in the mean velocity profile. This aspect is reflected in both rotating simulation cases in figure 2.8. The width of this linear region also grows larger with increasing rotation number, which correlates well with Kristofferson and Andersson (1993). As case A does not include rotational effects, the corresponding mean velocity profile is expectedly symmetric about the channel centerline ($y = 1$) and does not include a linear region.

2.4.2 Reynolds stresses, turbulent kinetic energy and dissipation rate

Figure 2.9: Reynolds-stress profiles: (a) $\overline{u'u'}$; (b) $\overline{v'v'}$; (c) $\overline{w'w'}$; (d) $\overline{u'v'}$. —: Case A; - - -: Case B; $\cdots$: Case C.

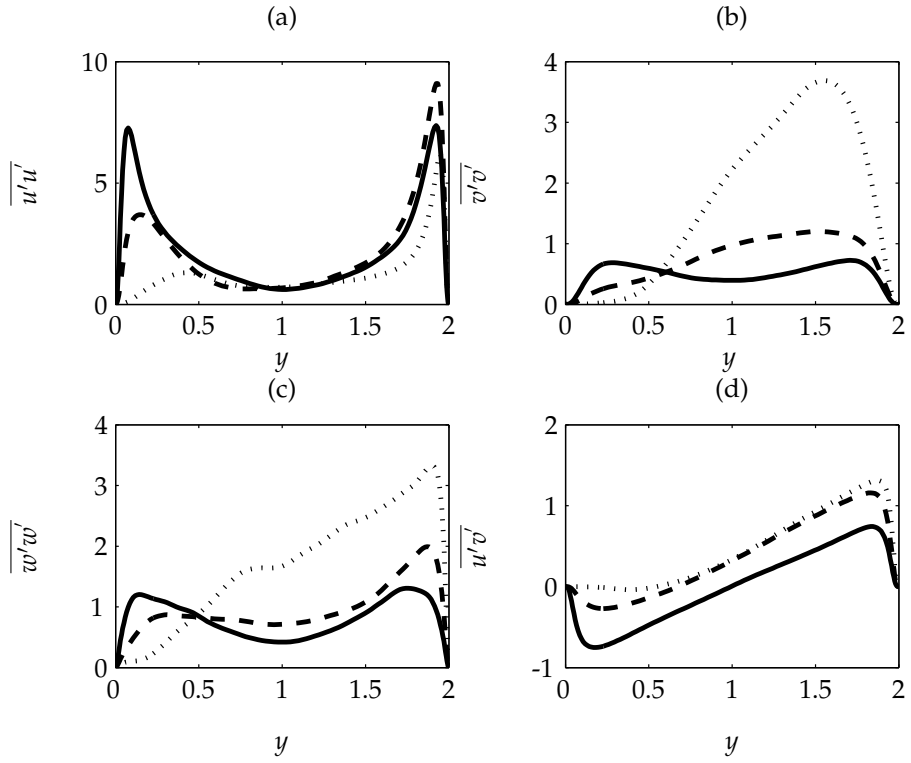

Reynolds-stresses profiles are shown in figure 2.9 for all rotation numbers. For cases involving rotation ($B - C$), the strength of the turbulence shifts towards the pressure side in figures 2.9$(b - d)$ as shown by the higher amplitudes of turbulent stresses in the region near the pressure wall ($y = 2$). This correlates with increased turbulence levels that would be expected in the pressure region due to the appearance of Taylor-Gortler vortices (roll cells) as described by Grundestam et al. (2008). There is also a subsequent decrease in the amplitudes of the turbulent normal stresses near the suction wall at $y = 0$, which correlate with the expected suppressed turbulence levels in the suction region. For $Ro_m = 0.1$, there is a slight increase in the peak value of $\overline{u'u'}$ on the pressure side of the channel, but this peak amplitude subsequently decreases at the high rotation number $Ro_m = 0.5$. In the profiles for $\overline{v'v'}$, an increasing rotation number results in an increase in

the peak value at $y = 1.5$. Similarly, when subject to rotation, the $\overline{w'w'}$ profiles display a consistent peak value at $y = 1.8$ that increases with the rotation number. The results of these simulations correspond well with Kristofferson and Andersson (1993), who found that at a rotation number of approximately $Ro_m = 0.2$, the levels of $\overline{u'u'}$ saturate near the pressure wall, and instead energy is distributed to the other Reynolds normal stresses components. In the DNS profiles for the shear stress $\overline{u'v'}$, the introduction of spanwise rotation in case B produces a constant positive offset from case A throughout the entire domain with exception of the near-wall region, with a slight positive amplitude increase as the rotation number increases further. These Reynolds stress profiles were consistent with the DNS results of Kristofferson and Andersson (1993) for all rotation numbers.

Figure 2.10: Total volume-averaged turbulent kinetic energy. —: Case A; - - -: Case B; · · ·: Case C.

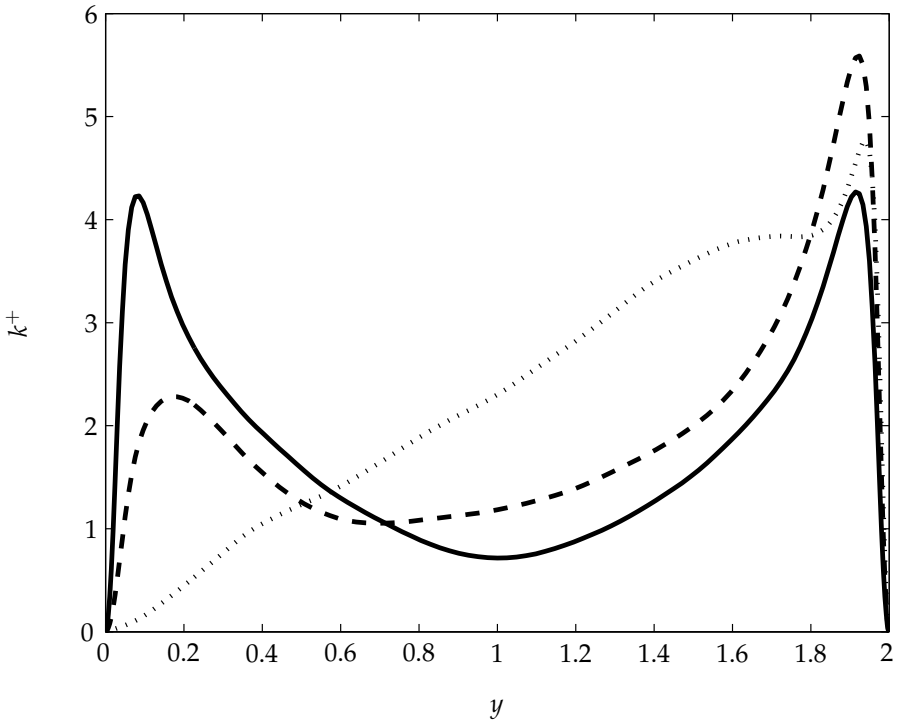

Figure 2.11: Turbulent dissipation rate ε. —: Case A; - - -: Case B; $\cdots$: Case C.

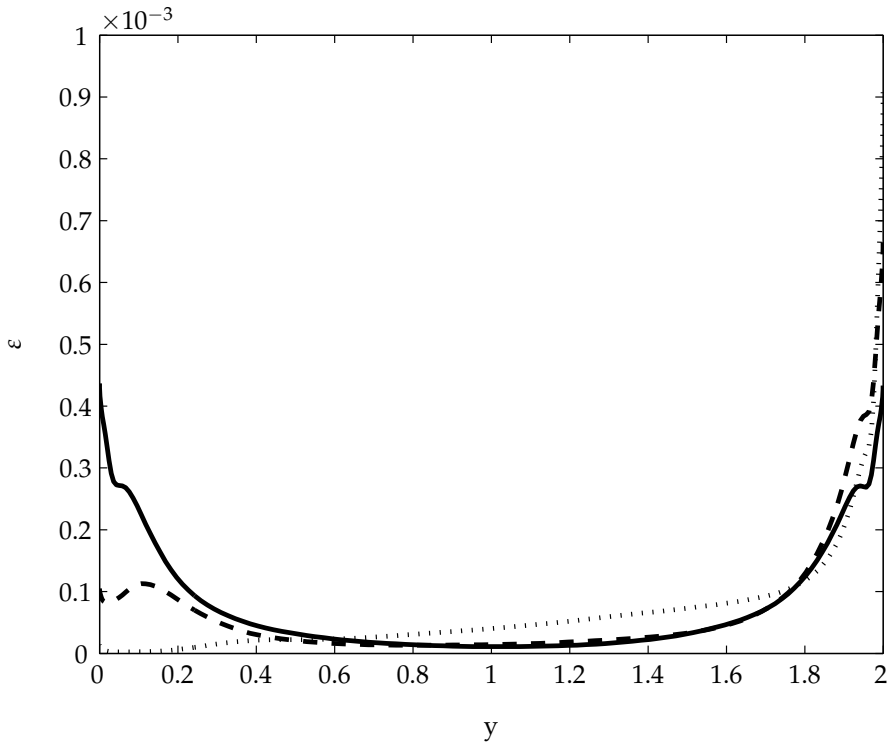

The distributions of the total volume-averaged turbulent kinetic energy k are shown in figure 2.10 for all rotation numbers. Similar to the present DNS distributions of the Reynolds-stresses for varying rotation numbers, the distribution of the turbulent kinetic energy across the channel is symmetric for non-rotating channel flow (case A); when rotation is introduced, the turbulent kinetic energy distribution becomes asymmetric, and the levels of turbulence are demonstrated to increase with increasing rotation number near the pressure wall ($y = 2$). The distributions of the turbulent dissipation rate ε are also displayed in figure 2.11, which similarly display asymmetry due to added rotation.

2.4.3 Velocity fluctuations

Various instantaneous streamwise and wall-normal velocity fluctuation contour plots at different rotation numbers are shown to assist visualization of the pressure and suction regions of the channel; colors within the contour plots represent the magnitudes of the respective velocity fluctu-

ations. Figure 2.12 shows the (x,y)-planes of instantaneous streamwise and wall-normal velocity at the spanwise coordinate $z/\delta = \pi$ for simulation case A. It is observed that turbulence is evenly distributed throughout the channel for both fluctuation velocities. Figures 2.13 and 2.14 show the same instantaneous velocity contour plots for simulation cases B and C, respectively, at the same spanwise coordinate. For low rotation number $Ro_m = 0.1$, figure 2.13(a) demonstrates that wall-normal velocity fluctuations are suppressed in the region nearest to the suction wall ($y = 0$) and high turbulence interactions are becoming restricted to the pressure region of the channel. The streamwise fluctuation contour plot shows a similar trend, but the suction region still contains long elongated structures. For the high rotation number $Ro_m = 0.5$, the wall-normal fluctuations become more concentrated into a series of small quasi-periodic structures on the pressure side of the channel, and turbulence is highly suppressed elsewhere. This same type of trend is also observable in the contour plots for the streamwise fluctuations. These figures collectively indicate that turbulence in spanwise-rotating turbulent channel flow is stratified in the wall-normal direction and the level of stratification increases as the rotation number grows larger. The Coriolis force increases with the rotation number, which forces fluid from the suction region into the pressure region, thus enhancing mixing and turbulence in pressure region while laminarizing the suction region where no mixing is occuring. Hence the enhanced and suppressed aspects of turbulence in the pressure and suction regions of the channel, respectively, are clearly seen in contour plots of streamwise and wall-normal instantaneous velocity.

Figure 2.12: Instantaneous velocity fluctuation contour plots ($Ro_m = 0$). (a) Streamwise (b) Wall-normal

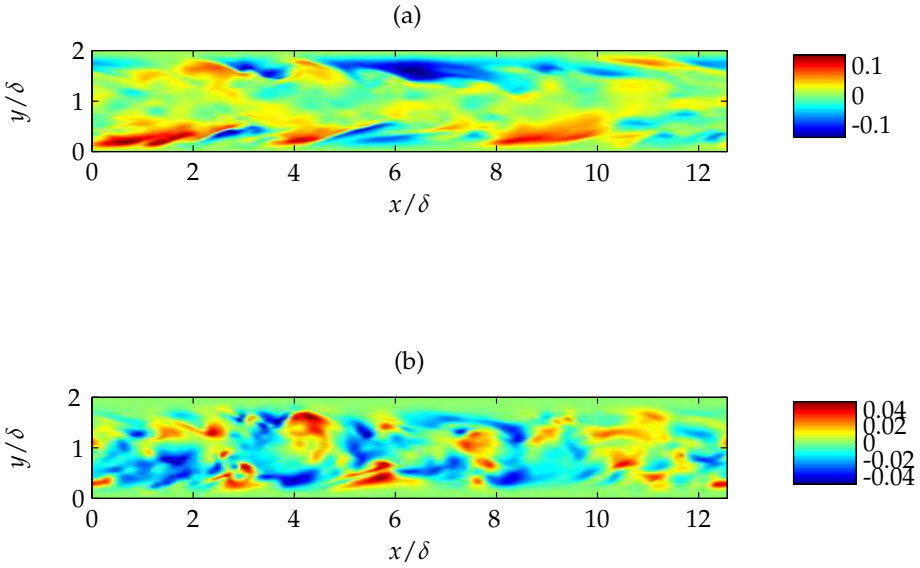

Figure 2.13: Instantaneous velocity fluctuation contour plots ($Ro_m = 0.1$). (a) Streamwise (b) Wall-normal

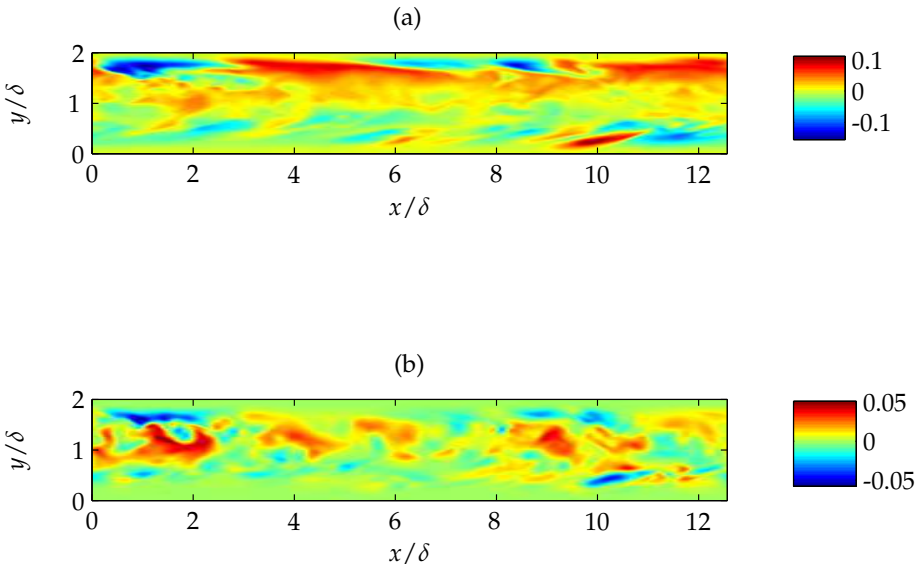

Figure 2.14: Instantaneous velocity fluctuation contour plots ($Ro_m = 0.5$). (a) Streamwise (b) Wall-normal

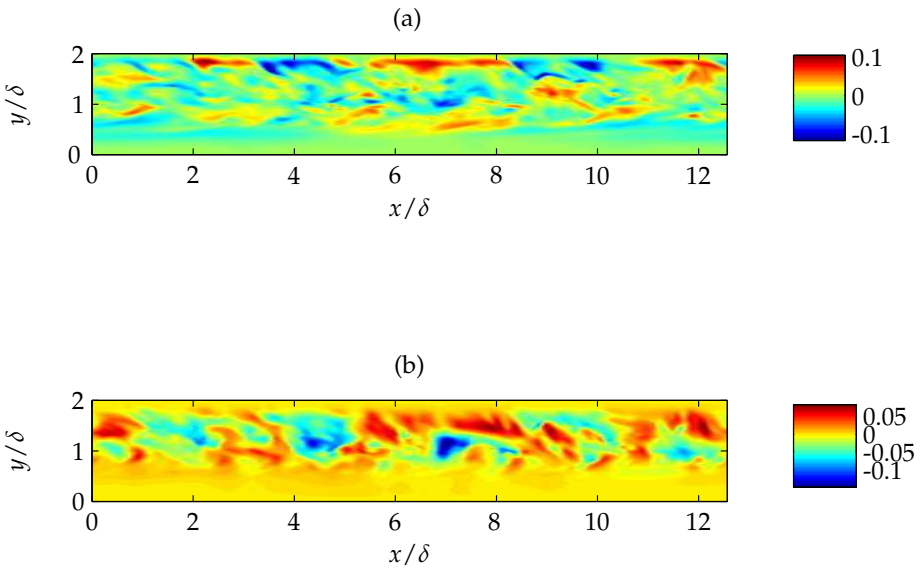

Chapter 3

RANS Turbulence Models

3.1 Turbulence Model Overview

Reynolds-Averaged Navier-Stokes (RANS) based turbulence models are based upon analyzing flows in two parts, an average (or mean) component and a fluctuating component. This concept of averaging is applied to the equations of mass and momentum conservation, producing terms known as the Reynolds stresses. The modeling of these Reynolds stresses is the primary objective of RANS-based models, which must solve the turbulence closure problem associated with these equations. One of the most common methods within these RANS-based models to obtain closure is to relate the Reynolds stresses linearly to the mean strain rate tensor S_{ij} through the definition of an "eddy" viscosity. However, these models, known as linear eddy viscosity models, have been known to fail significantly in complex flows, including rotational flows. Nonlinear eddy viscosity models have also been developed, which use a nonlinear relationship between the Reynolds stresses, mean strain rate and rotation tensors in order to more accurately model complex flows; unfortunately, a constitutive relationship between the Reynolds stress and mean velocity gradient has been demonstrated to not exist in turbulence (Lumley, 1970). This work considers three nonlinear eddy viscosity models: the $\overline{v^2} - f$, SG and Girimaji turbulence models, proposed by Reif, Durbin, and Ooi (1999), Speziale and Gatski (1993), and Girimaji (1996), respectively.

In this section, three RANS models are being tested due to their practical computational costs and popularity in the engineering community. However, the deficiencies of RANS models must be considered especially the information that is lost from the results of RANS modeling

compared to that of a direct numerical simulation. As mentioned above, RANS models apply the notion of averaging to the Navier-Stokes equations, which eliminates phase information and retains only amplitude information from the governing equations of the flow. Phase information has a plethora of uses in fluid mechanics research as it includes data such as the pressure signals at the channel walls, which are crucial information in research areas such as flow control as many methods of flow control design are centered about a certain frequency range. Therefore the results obtained from RANS modeling would be useless to researchers in need of this information even if the results obtained from the RANS model were very accurate relative to DNS data.

3.1.1 $\overline{v^2} - f$ turbulence model

The $\overline{v^2} - f$ turbulence model is similar to many linear eddy viscosity models in which partial differential equations for the turbulent kinetic energy k and turbulent dissipation energy rate ε, shown in equations 3.1 and 3.2, are solved. This model also incorporates the two additional partial differential equations in equations 3.3 and 3.4, for $\overline{v^2}$ and f, which correspond to a scalar analogous to the wall-normal Reynolds stress and an elliptic relaxation function, respectively. These equations (eq. 3.1 - 3.4) are also a function of the production term (P), kinematic viscosity (ν), eddy viscosity (ν_t), turbulent length scale (L), and turbulent time scale (T); the model coefficients are shown in table 3.1. The model expressions for the turbulent length and time scales are found in equation 3.5.

$$\frac{Dk}{Dt} = P - \varepsilon + \frac{\partial}{\partial x_j}((\nu + \nu_t)\frac{\partial k}{\partial x_j}) \tag{3.1}$$

$$\frac{D\varepsilon}{Dt} = \frac{C^*_{\epsilon 1}P - C_{\epsilon 2}\varepsilon}{T} + \frac{\partial}{\partial x_j}((\nu + \frac{\nu_t}{\sigma_\epsilon})\frac{\partial \varepsilon}{\partial x_j}) \tag{3.2}$$

$$\frac{D\overline{v^2}}{Dt} = kf - \frac{\overline{v^2}}{k} + \frac{\partial}{\partial x_j}((\nu + \nu_t)\frac{\partial \overline{v^2}}{\partial x_j}) \tag{3.3}$$

$$f - L^2\nabla^2 f = (C_1 - 1)\frac{2/3 - \overline{v^2}/k}{k} + C_2\frac{P}{k} \tag{3.4}$$

$$L = C_L\, max(\frac{k^{3/2}}{\varepsilon};\, C_\eta(\frac{\nu^3}{\varepsilon})^{1/4})\,,\quad T = max(\frac{k}{\varepsilon};\, 6(\frac{\nu}{\varepsilon})^{1/2}) \tag{3.5}$$

Table 3.1: Coefficients for the $\overline{v^2} - f$ Model (Reif et al., 1999)

$C^*_{\epsilon 1}$	$C_{\epsilon 2}$	σ_ϵ	C_L	C_η
$1.4\ (1 + 0.045\ \sqrt{\frac{f}{\overline{v^2}}})$	1.9	1.3	0.25	85.0

By solving equations 3.1 - 3.4, the $\overline{v^2} - f$ model produces an explicit expression for the Reynolds stresses shown in equation 3.6, where C^*_μ is a function of the strain rate (S_{ij}) and rotation tensors (W_{ij}). More information on the $\overline{v^2} - f$ model's formulation and derivation is found in the appendices.

$$\overline{u'_i u'_j} = \frac{2}{3} k \delta_{ij} - 2 C^*_\mu \overline{v^2} T S_{ij} \tag{3.6}$$

3.1.2 Speziale-Gatski turbulence model

The Speziale-Gatski model, or SG model, is an explicit algebraic Reynolds stress model (EARSM), a common subtype of nonlinear eddy viscosity models. In EARSM-type models, an implicit model for the anisotropic tensor b_{ij} is constructed from the Reynolds stress equation and then an explicit form for b_{ij} is derived analytically. Using the relationship between the anistropic tensor and Reynolds stress tensor shown in equation 3.7 (Pope, 1975), the SG model proposes the following explicit expression for the Reynolds stresses in equation 3.8. The model coefficients are found in table 3.2, and it is important to note the non-absolute nature of several coefficients. The terms η and ζ are equivalent to invariants of the scaled strain rate and rotation tensors, or $S_{ij}S_{ij}$ and $W_{ij}W_{ij}$, respectively; similarly, Π_b represents the second invariant of the anisotropic tensor, $b_{ij}b_{ij}$. Model expressions for α_1, S_{ij}, and W_{ij} are found in equations 3.9, 3.10, and 3.11, respectively, with $\overline{S}_{ij}$ and $\overline{w}_{ij}$ representing the dimensional strain rate and rotation tensors, respectively. Additionally, the SG model applies the partial differential equations used in the $\overline{v^2} - f$ model and shown in equations 3.1 and 3.2 to compute the turbulent kinetic energy k and dissipation rate ε. For more information on the SG turbulence model and its formulation and derivation, readers are

Table 3.2: Coefficients for the SG Model (Speziale and Gatski, 1993)

C_1	C_2	C_3	C_4	g
3.4 + 1.8 P/ε	0.8 - 1.3 Π_b	1.25	0.40	0.233

referred to the appendices.

$$b_{ij} = \frac{\overline{u_i' u_j'}}{2k} - \frac{1}{3}\delta_{ij} \tag{3.7}$$

$$\overline{u_i' u_j'} = \frac{2}{3}k\delta_{ij} - \frac{6(1+\eta^2)\alpha_1 k}{3+\eta^2+6\zeta^2\eta^2+6\zeta^2}(S_{ij} + S_{ij}W_{kj} - W_{ik}S_{kj}) - 2(S_{ik}S_{kj} - \frac{1}{3}S_{mn}S_{mn}\delta_{ij}) \tag{3.8}$$

$$\alpha_1 = \frac{C_2 - 4/3}{C_3 - 2} \tag{3.9}$$

$$S_{ij} = \frac{1}{2}g\frac{k}{\varepsilon}(2 - C_3)\overline{S}_{ij} \tag{3.10}$$

$$W_{ij} = \frac{1}{2}g\frac{k}{\varepsilon}(2 - C_4)[\overline{w}_{ij} + (\frac{C_4 - 4}{C_4 - 2})e_{mji}\Omega_m] \tag{3.11}$$

3.1.3 Girimaji turbulence model

The Girimaji turbulence model is also an EARSM-type model and its basic formulation is very similar to that of the SG model. The primary difference from the SG model occurs once the implicit model for the anistropic tensor is constructed consisting of nonlinear algebraic equations derived from the Reynolds stress equation. With the amount of unknowns exceeding the amount of equations in the Reynolds stress equation causing the well-known turbulence "closure" problem, these two models resolve this "closure" problem using different methods. The SG model uses mathematical functions known as Pade approximants to reduce the number of unknowns and form a regularized, or approximated, model that relates the anisotropic, strain rate and rotation tensors. Alternatively, the Girimaji model fully solves the nonlinear equations under an imposed "weak equilibrium" assumption which presumes a constant ratio between the production and dissipative energy rate budget terms. More information regarding these models' solutions to

Table 3.3: Coefficients for the Girimaji Mode (Girimaji, 1996)

L_{01}	L_{11}	L_2	L_3	L_4
0.70	3.8	-0.4867	-0.375	-0.8

the closure problem is found in the appendices. The explicit expression for the Girimaji-modeled Reynolds stresses is shown in equation 3.12. The coefficients of the Girimaji model are found in table 3.3, and it is noted that all of the coefficients are absolute. Similar to the SG model, the terms η_1 and η_2 represent invariants of the normalized strain rate and rotation tensors: $S_{ij}S_{ij}$ and $W_{ij}W_{ij}$, respectively, and in this case these tensors are scaled by the eddy turnover time k/ε. The expressions for the G coefficients are shown in equations 3.13 and 3.14; the various dependencies of these terms, such as model parameters D and b, are found in the appendices. For more detail regarding the formulation and derivation of the Girimaji turbulence model, readers are referred to the appendices.

$$\overline{u_i'u_j'} = 2k(G_1S_{ij} + G_2(S_{ik}W_{kj} + W_{ik}S_{kj}) + G_3(S_{ik}S_{kj} - \frac{1}{3}S_{mn}S_{mn}\delta_{ij})) - \frac{2}{3}k\delta_{ij} \tag{3.12}$$

$$G_1 = \begin{cases} \frac{L_{01}L_2}{L_{01}^2+2\eta_2 L_4^2} & \text{when } \eta_1 = 0 \\ -\frac{p}{3} + (-\frac{b}{2} + \sqrt{D})^{1/3} + (-\frac{b}{2} - \sqrt{D})^{1/3} & \text{when } D > 0 \\ -\frac{p}{3} + 2\sqrt{-\frac{a}{3}}\cos(\frac{\theta}{3}) & \text{when } D < 0 \text{ and } b < 0 \\ -\frac{p}{3} + 2\sqrt{-\frac{a}{3}}\cos(\frac{\theta}{3} + \frac{2\pi}{3}) & \text{when } D < 0 \text{ and } b > 0 \end{cases} \tag{3.13}$$

$$G_2 = -\frac{L_4G_1}{L_{01}^2 - \eta_1 L_{11}G_1}$$
$$G_3 = -\frac{L_4G_1}{L_{01}^2 - \frac{2}{3}\eta_2 L_3 + \eta_1 L_{11}G_1} \tag{3.14}$$

3.2 RANS Model Testing

As noted in the previous section, the three RANS-based models in this work are all nonlinear eddy viscosity models, and so the approximations for the Reynolds stresses in these models are various functions of the mean strain rate tensor, rotation tensor, turbulent kinetic energy and dissipation rate. When these turbulence models are used for predictive purposes, partial differential equations of the velocity, turbulent kinetic energy, and dissipation rate are numerically solved to yield these quantities. However, since the purpose of this work is to test the *modeling* capabilities of these three turbulence models, these implemented quantities will be directly extracted from the DNS data base, thus yielding more accurately modeled Reynolds stresses for comparison with the Reynolds stresses directly extracted from the DNS.

The normal Reynolds stresses ($\overline{u_i' u_i'}$) and shear Reynolds stress ($\overline{u' v'}$) calculated from the DNS data using the three aforementioned turbulence models are compared directly to the results of the DNS for the three rotation numbers used in the present DNS study. For a case of non-rotation (A), the results are shown in figure 3.1. The approximations of the SG and Girimaji models are similar, and more accurately model the Reynolds normal stresses compared to the $\overline{v^2} - f$ model; the $\overline{v^2} - f$ model has the most accurate distribution of the Reynolds shear stress, however. It is important to note that there are slight irregularities in the Girimaji-modeled Reynolds normal stresses and a significant discontinuity in the Girimaji-modeled Reynolds shear stress at the channel center-line.

Figure 3.1: Modeled Reynolds stresses profiles ($Ro_m = 0$): (a) $\overline{u'u'}$; (b) $\overline{v'v'}$; (c) $\overline{w'w'}$; (d) $\overline{u'v'}$. —: DNS; $\cdots$: $\overline{v^2} - f$; - · -: SG; - - -: Girimaji.

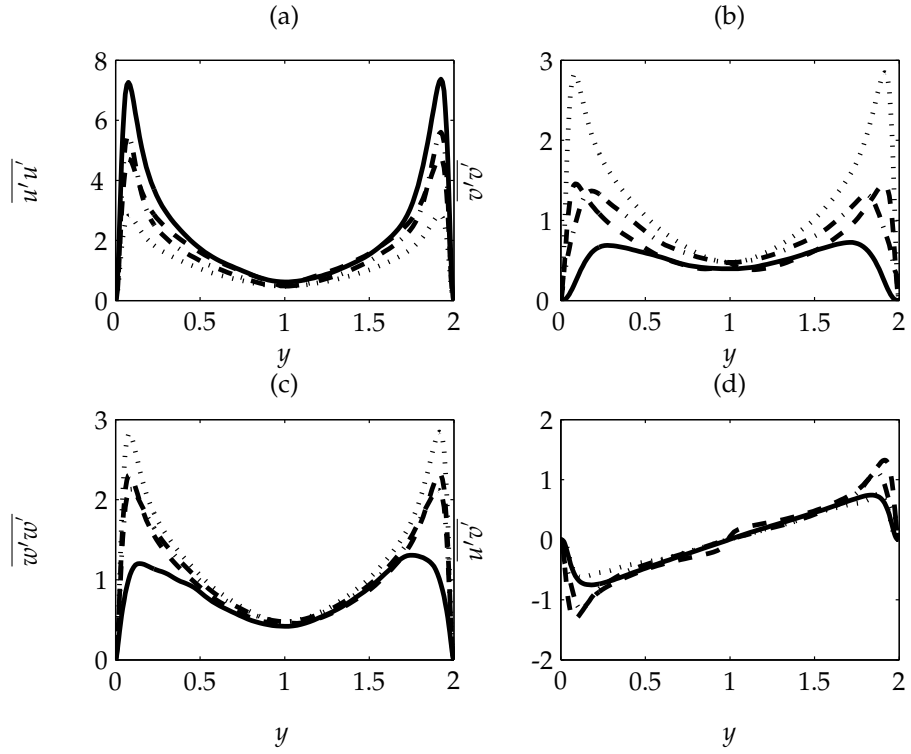

For low rotation number (case B), the modeled Reynolds stresses and DNS results are plotted in figure 3.2, and for high rotation number (case C), the results are shown in figure 3.3. It is observed that once rotational effects are considered in the Girimaji turbulence model, the discontinuity and irregularities disappear from its modeled Reynolds stresses. For the cases involving rotation, the SG model generally produces the most accurate modeled Reynolds stresses compared to the distributions directly obtained from the DNS data.

Figure 3.2: Modeled Reynolds stresses profiles ($Ro_m = 0.1$): (a) $\overline{u'u'}$; (b) $\overline{v'v'}$; (c) $\overline{w'w'}$; (d) $\overline{u'v'}$. —: DNS; $\cdots$: $\overline{v^2} - f$; - · -: SG; - - -: Girimaji.

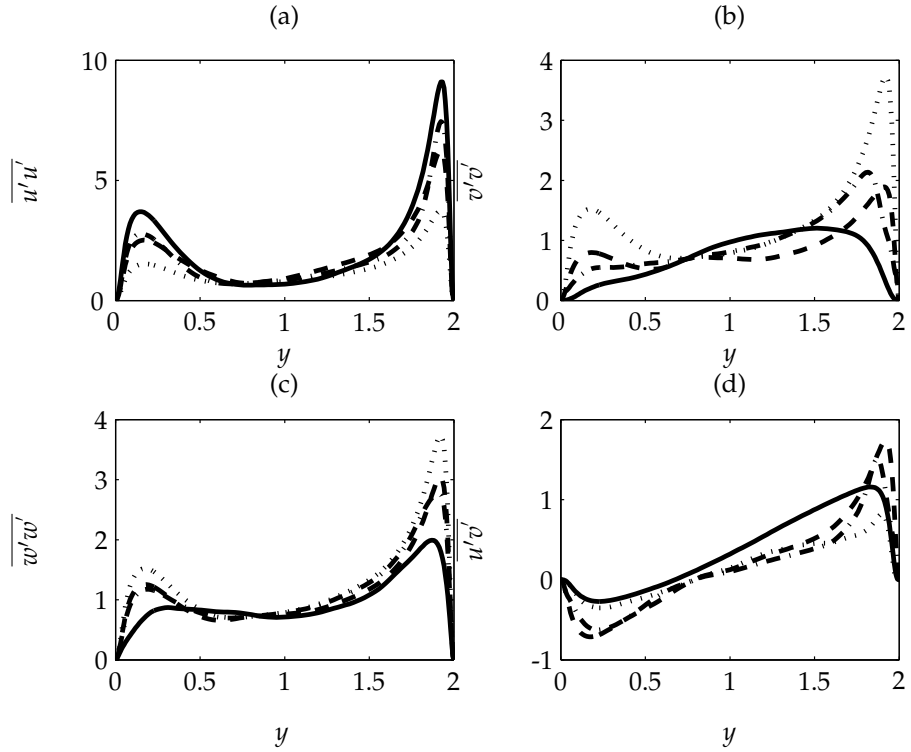

Figure 3.3: Modeled Reynolds stresses profiles ($Ro_m = 0.5$): (a) $\overline{u'u'}$; (b) $\overline{v'v'}$; (c) $\overline{w'w'}$; (d) $\overline{u'v'}$. —: DNS; $\cdots$: $\overline{v^2} - f$; - · -: SG; - - -: Girimaji.

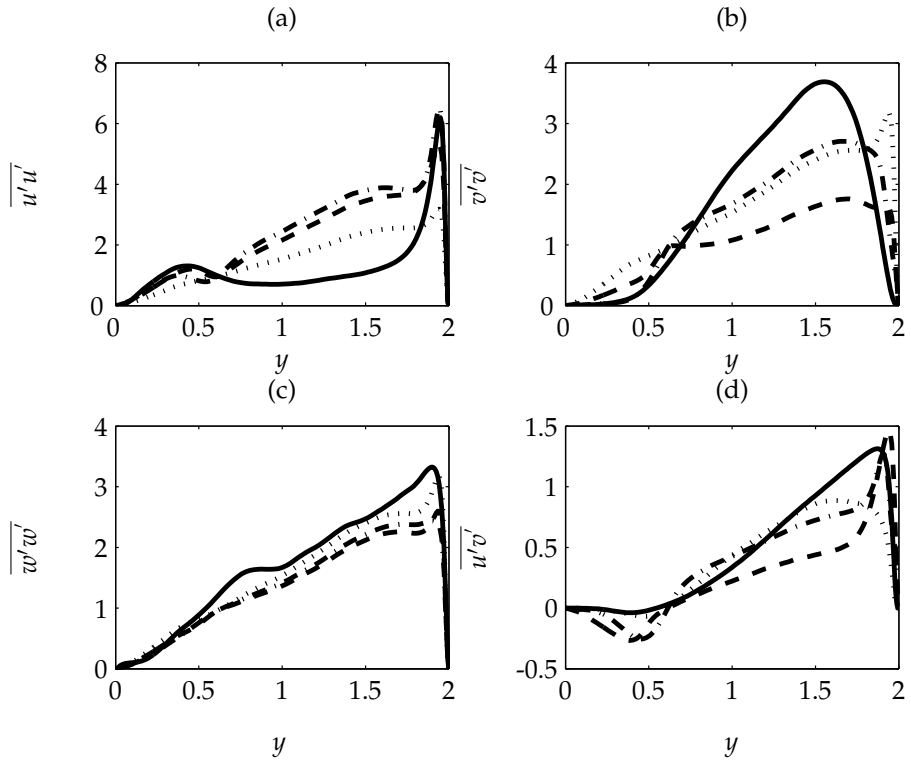

3.3 Girimaji Model Correction

In this section, the aforementioned discontinuity in the Girimaji-modeled Reynolds shear stress profile in the non-rotational case (A) is removed by adding a corrective function to the turbulence model. The explicit expression for the Reynolds stresses in equation 3.12 is examined for the dominant influences on the modeled Reynolds shear stress term. The various groupings on the right hand-side (RHS) of equation 3.12 are individually plotted for each G coefficient in figure 3.4, and the grouping composed the G_1 coefficient, turbulent kinetic energy k and mean strain rate tensor S_{12} is found to be the primary contributor to the modeled Reynolds shear stress. No anomalies are present in the distributions of k in figure 2.10 and S_{12} in figure 3.5, so it is concluded that the G_1 coefficient is the primary cause of the discontinuity. The G_1 coefficient has a strong dependency on η_1, whose distribution is plotted in figure 3.6 and shown to approach zero at the

channel center-line. An inspection of the Girimaji model parameters shows an inverse relationship between η_1 and G_1, which would cause the values of G_1 to be elevated significantly near the channel center-line where η_1 approaches zero. This combination of elevated magnitudes of the G_1 coefficient and a change of sign in the S_{12} tensor produces the discontinuity at the channel center-line for modeled Reynolds shear stress. Therefore, this discontinuity is attributed to a deficiency in the G_1 coefficient expressions as $\eta_1 \to 0$.

Figure 3.4: G coefficient groupings within the Girimaji-modeled Reynolds shear stress ($Ro_m = 0$). —: G_1; - - -: G_2; - · -: G_3.

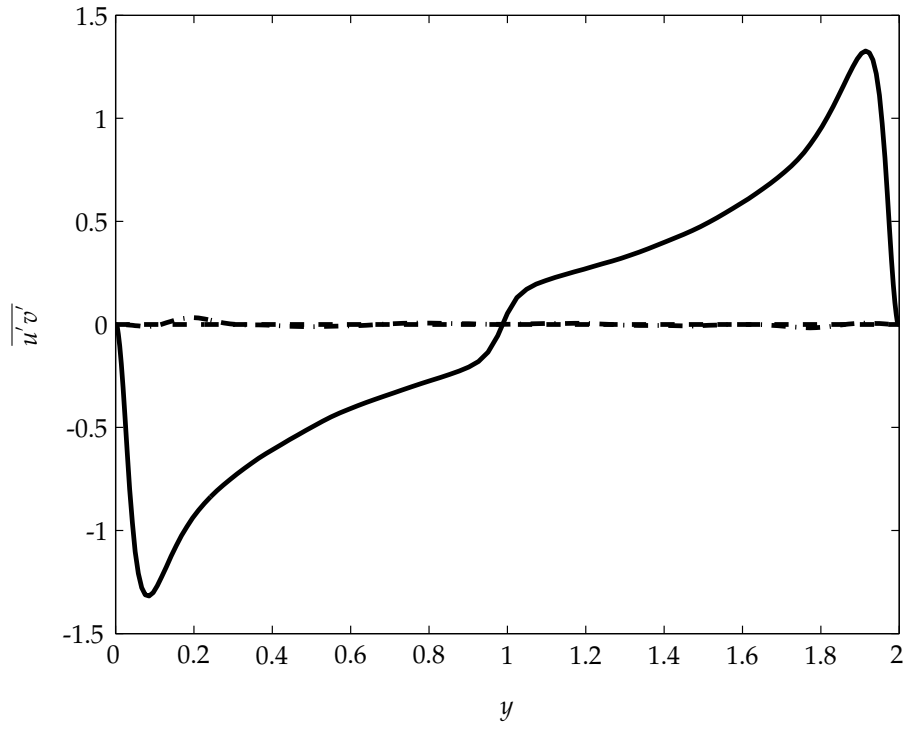

Figure 3.5: Mean strain rate tensor distribution ($Ro_m = 0$).

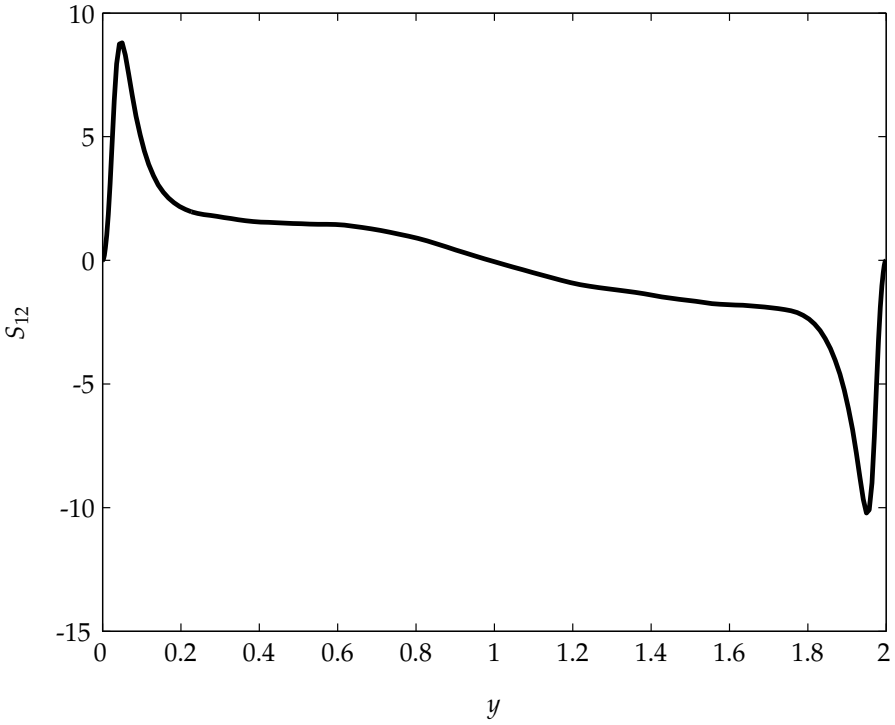

Figure 3.6: η_1 distribution in the Girimaji model ($Ro_m = 0$).

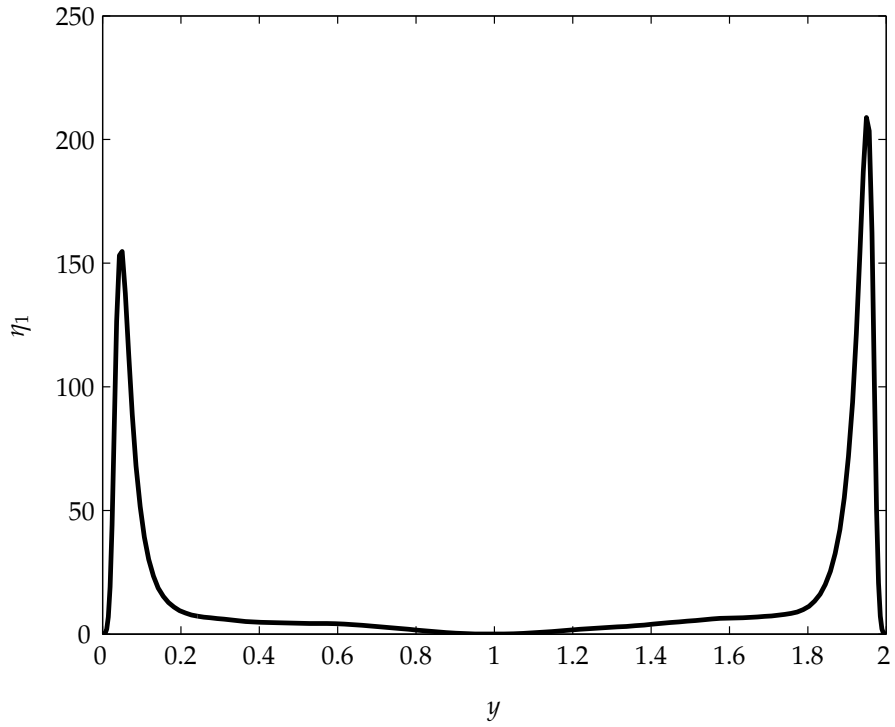

The Girimaji model has an alternate expression for G_1 at $\eta_1 = 0$ as shown in equation 3.13. However, this equation is shown in figure 3.7 to have similar values to the regular G_1 coefficient used, including in the region of the discontinuity. Consequently, the substitution of this expression into the model would not alter the value of the modeled Reynolds shear stress enough to reduce or eliminate the discontinuity. Figure 3.7 also displays the expected large magnitudes of the G_1 coefficient near the channel center-line relative to the rest of the channel. A correction to the Girimaji model is made by introducing a new limiting value for the G_1 coefficient as η_1 approaches zero. Through analysis and comparison of the profiles for the G_1 coefficient and η_1, an adequate value of G_1 was determined for a certain span of values of η_1 that evened out the discontinuity. A corrective value for G_1 of -0.15 corresponding to values of $\eta_1 \leq 2.0$ was assigned to the Girimaji model as shown in equation 3.15, which produced the following $\overline{u'v'}$ profile shown in figure 3.8 and the G_1 coefficient profile in figure 3.7.

$$G_1 = -0.15 \text{ for } \eta_1 \leq 2.0 \tag{3.15}$$

Figure 3.7: G_1 coefficient in the Girimaji model ($Ro_m = 0$). —: Original; - - -: With corrective function; $\cdots$: Girimaji model expression for $\eta_1 = 0$.

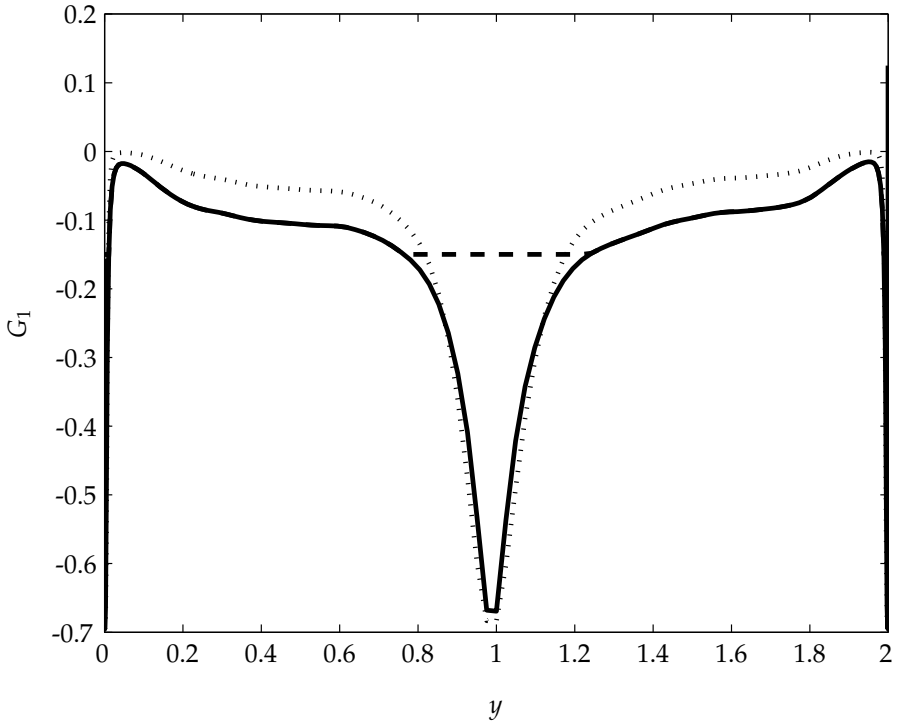

Figure 3.8: Girimaji-modeled Reynolds shear stress profile ($Ro_m = 0$). —: DNS; - · -: Prediction with correction; · · ·: Prediction without correction.

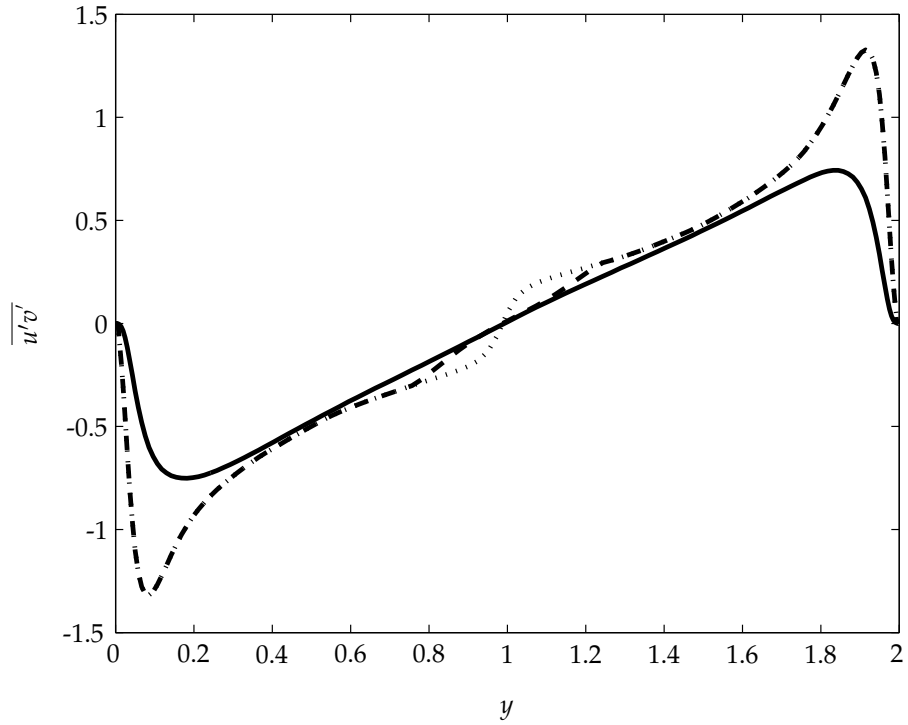

As demonstrated in figure 3.8, the discontinuity is evened out in the modeled shear Reynolds stress profile and a more accurate slope in relation to the DNS data is displayed compared to the original Girimaji-modeled $\overline{u'v'}$ profile. This correction was unable to eliminate the slight irregularities present in the modeled Reynolds normal stresses in the Girimaji model. However, as shown in equation 3.12, the modeled Reynolds normal stresses have a greater dependency on the coefficients G_2 and G_3, therefore a similar analysis can be applied for those coefficients to eliminate the irregularities at the channel center-line in those profiles.

Realizability is a set of mathematical and physical principles that need to be satisfied to prevent the turbulence model from generating non-physical results. The three realizability conditions demonstrated by Schumann (1977) are shown in equations 3.16 - 3.18.

$$\overline{u_i' u_i'} \geq 0 \tag{3.16}$$

$$\overline{u_i' u_j'}^2 \leq \overline{u_i' u_i'}\,\overline{u_j' u_j'} \tag{3.17}$$

$$det(\overline{u_i' u_j'}) \geq 0 \tag{3.18}$$

Realizability testing of the Girimaji model with the proposed correction was conducted and distributions corresponding to the conditions in equations 3.16, 3.17 and 3.18 are shown in figures 3.9, 3.10 and 3.11, respectively. Figures 3.9(a) - (c) demonstrate that the modeled Reynolds normal stress distributions are non-negative which satisfies equation 3.16. Figure 3.10 displays the inequality in equation 3.17, also known as Schwartz's inequality, and the expression is shown to hold true. Finally, figure 3.11 demonstrates that the determinant of the modeled Reynolds stress tensor is non-negative, which satisfies the condition in equation 3.18; consequently the ad-hoc correction to the Girimaji model was established to satisfy all three realizability conditions.

Figure 3.9: Girimaji-modeled Reynolds-stress distributions with correction ($Ro_m = 0$). (a) $\overline{u'u'}$; (b) $\overline{v'v'}$; (c) $\overline{w'w'}$; (d) $\overline{u'v'}$.

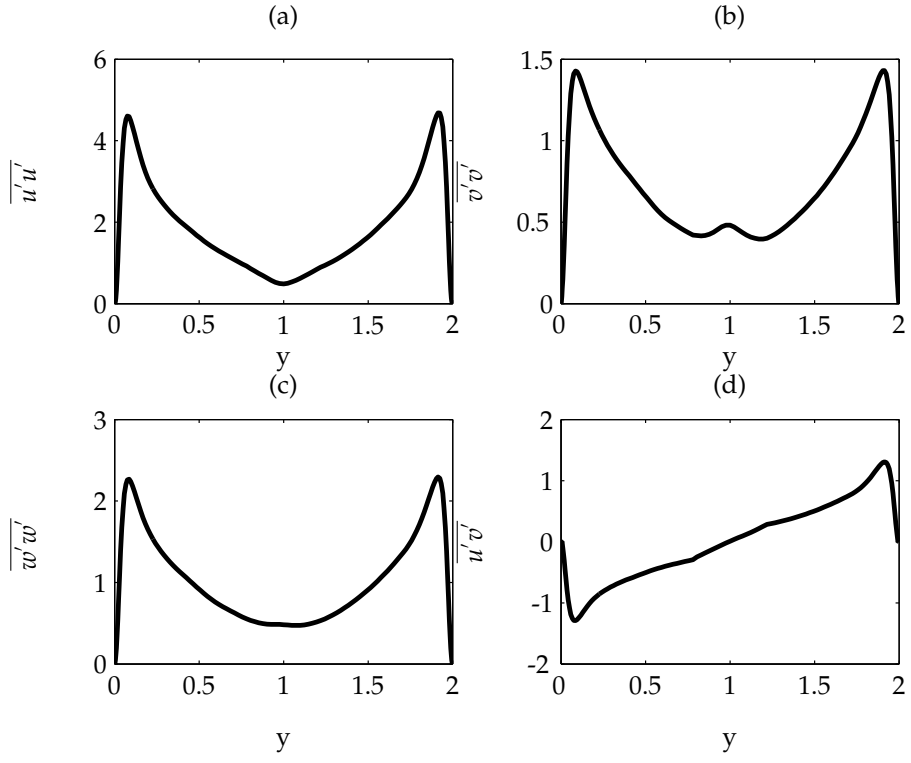

Figure 3.10: Girimaji-modeled Reynolds stress distributions for equation 3.17 [Schwartz's inequality] ($Ro_m = 0$). —: $\overline{u_1' u_2'}^2$; - - -: $\overline{u_1' u_1'}\,\overline{u_2' u_2'}$.

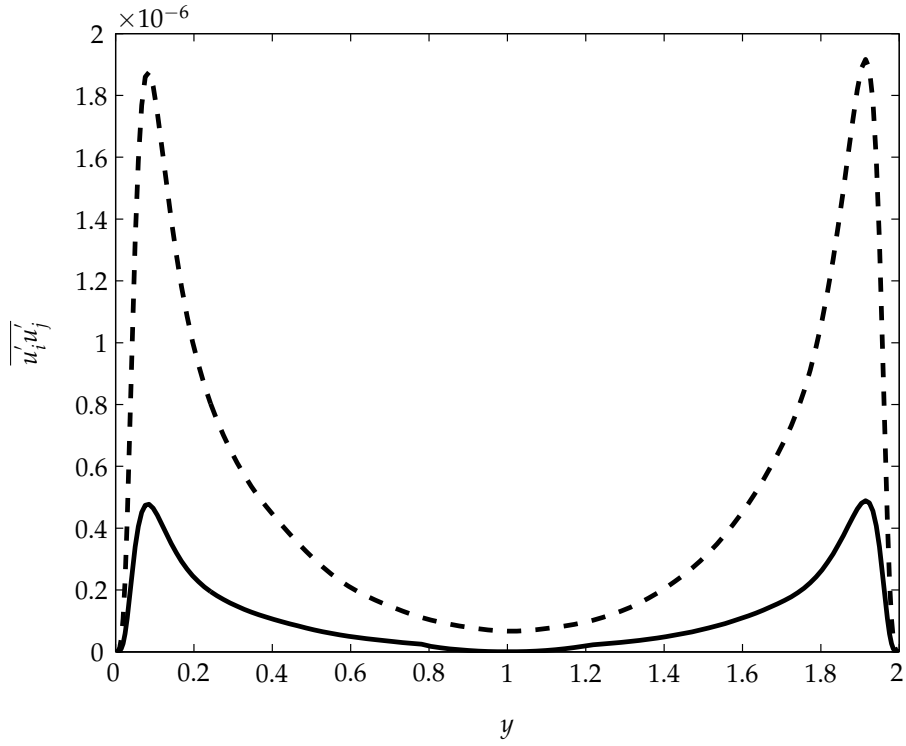

Figure 3.11: Determinant of Girimaji-modeled Reynolds stress tensor ($Ro_m = 0$).

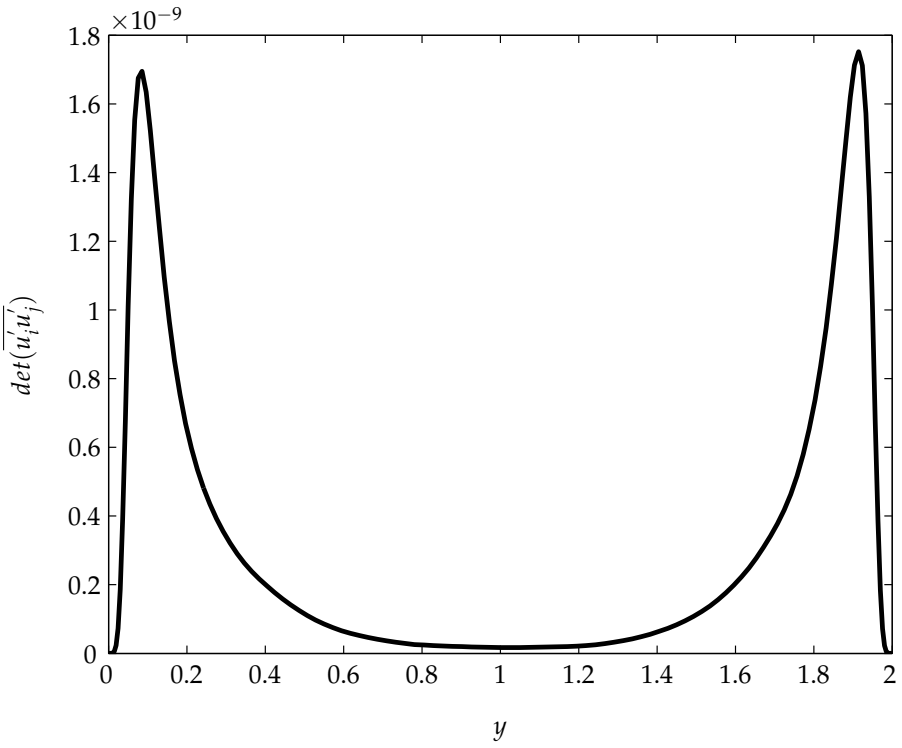

Chapter 4

Pressure-Strain Modeling in Explicit Algebraic Reynolds Stress Models

4.1 Pressure-Strain Overview

As the SG and Girimaji turbulence models have been demonstrated to have usefulness in modeling the Reynolds stresses in spanwise-rotating turbulent channel flows, a closer examination of these models can yield useful information on the influences of various model terms on the accuracy of the modeled Reynolds stresses. The SG and Girimaji models are both EARSM-type models, which utilize the Reynolds stress equation (eq. 4.1) by modeling the higher order terms (budget terms) that appear in that equation. The budget term variables listed in equation 4.1 include the pressure-strain term (Φ_{ij}), dissipation term (ε_{ij}) and pressure diffusion term (D_{ij}^T); R_{ij} is equivalent to $\overline{u_i' u_j'}$.

$$\frac{DR_{ij}}{Dt} = -R_{ik}\frac{\partial u_j}{\partial x_k} - R_{jk}\frac{\partial u_i}{\partial x_k} + \Phi_{ij} - \varepsilon_{ij} - 2\Omega_m(e_{mkj}R_{ik} + e_{mki}R_{jk}) + D_{ij}^T + \nu\nabla^2 R_{ij} \tag{4.1}$$

$$\Phi_{ij} = \overline{p(\frac{\partial u_i}{\partial x_j} + \frac{\partial u_j}{\partial x_i})} \tag{4.2}$$

$$\Pi_{ij} = -C_1\epsilon b_{ij} + C_2 k S_{ij} + C_3 k(b_{ik}S_{kj} + S_{ik}b_{kj} - \frac{2}{3}b_{mn}S_{mn}\delta_{ij}) - C_4 k(b_{ik}W_{kj} - W_{ik}b_{kj}) \tag{4.3}$$

In these models, the pressure-strain term (eq. 4.2) is of paramount importance as the correlations between pressure and strain fluctuations play a dominant role in intercomponent energy transfer (Launder, Reece, and Rodi, 1975). Consequently, the distributions of the pressure-strain function for each of these models are compared to the pressure-strain budget values directly extracted from the DNS simulations. Both of these models apply the linear Speziale, Sarkar, and

Gatski (SSG) pressure strain function (eq. 4.3), albeit with different sets of coefficients, so the modeled pressure-strain terms are examined for accuracy in regards to turbulent channel flow subject to spanwise rotation. Information on the intercomponent energy transfer in the Reynolds stress equation, especially concerning the pressure-strain, is eludicated further in the appendices.

4.2 Pressure-Strain Model Testing

An analysis is performed to assess the accuracy of the pressure-strain function shown in equation 4.3 for both the SG and Girimaji models in all three cases. Similar to the model testing for the Reynolds stresses, the quantities of the turbulent kinetic energy and dissipation rate used in model implementation of the pressure-strain were extracted directly from the DNS. For the non-rotating case (A), the modeled pressure-strain budget term values are compared with the results of the DNS in figure 4.1. It is demonstrated in figure 4.1 that the modeled pressure-strain function values for both models are very similar to the DNS values with the exception of the near-wall regions $0 \leq y \leq 0.2$ and $1.8 \leq y \leq 2$. This discrepancy in the near-wall regions is not unexpected as most pressure-strain models such as the SSG function are meant to model pressure-strain fluctuations in homogeneous turbulence, and are therefore often unable to independently model near-wall effects in turbulent flows. For rotating cases B and C, the modeled pressure-strain budget term values are compared with the results of the DNS in figures 4.2 and 4.3, respectively.

Figure 4.1: Pressure-strain budget term profiles ($Ro_m = 0$). —: DNS; - - -: SG; · · ·: Girimaji.

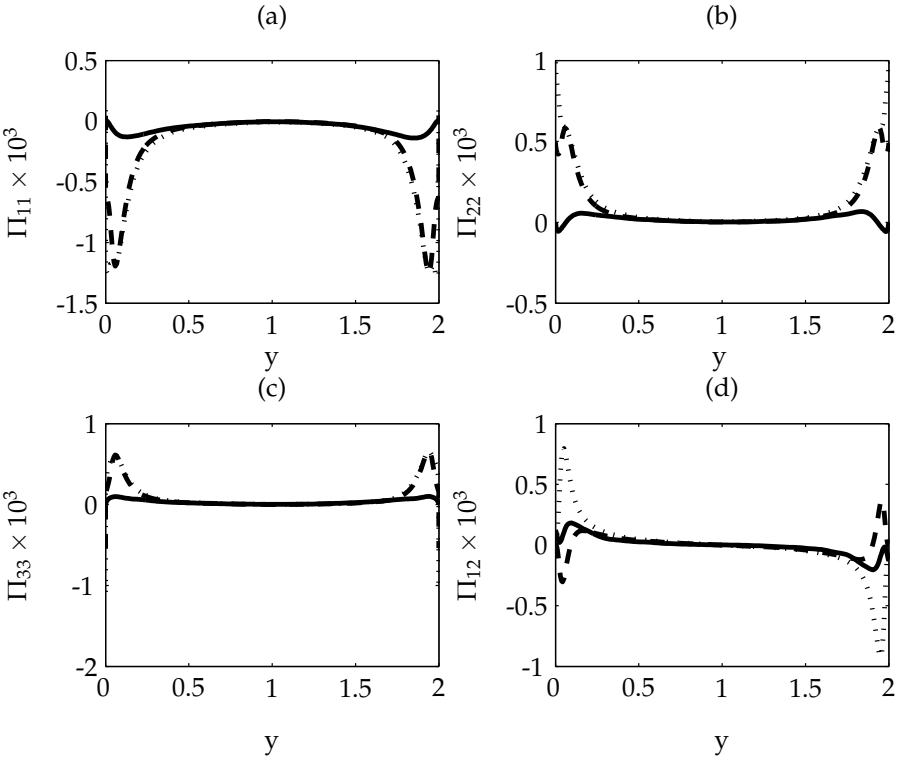

Figure 4.2: Pressure-strain budget term profiles ($Ro_m = 0.1$). —: DNS; - - -: SG; · · ·: Girimaji.

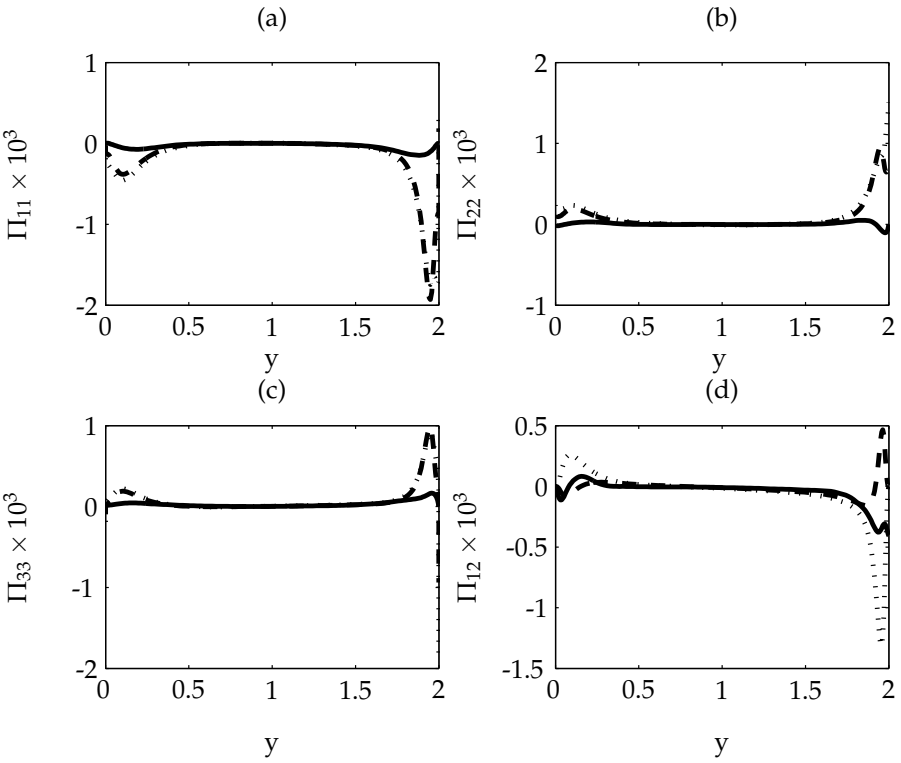

Figure 4.3: Pressure-strain budget term profiles ($Ro_m = 0.5$). —: DNS; - - -: SG; $\cdots$: Girimaji.

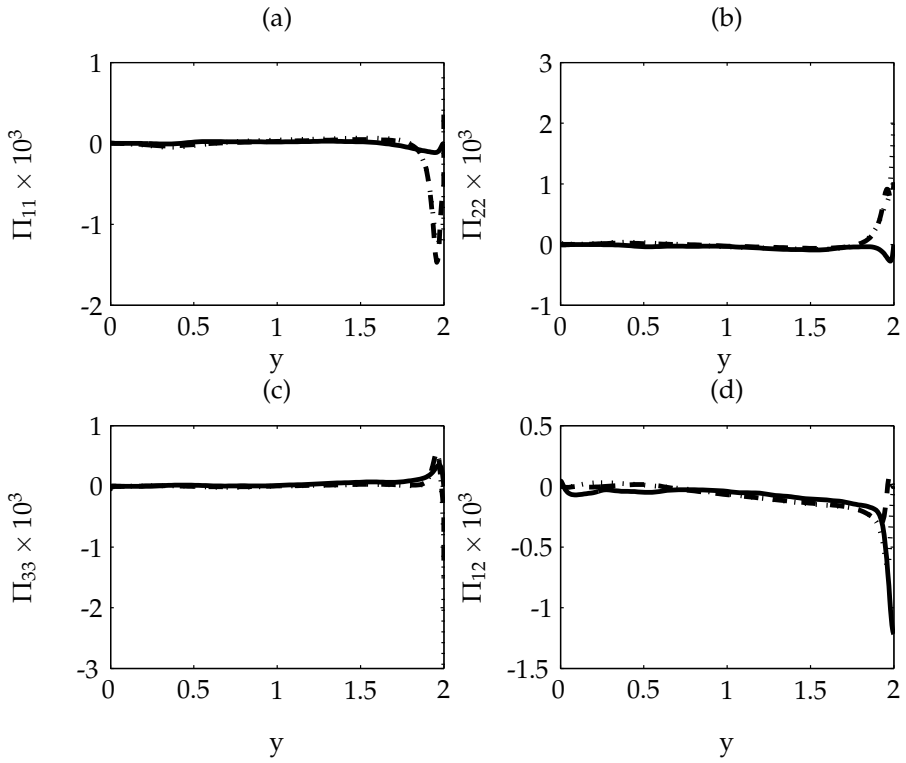

It is observed that the accuracy of the modeled pressure-strain increases with increasing rotation number near the suction wall ($y = 0$). At the highest rotation number, the modeled pressure-strain values are much more accurate with respect to the DNS compared to the non-rotational case, and the only major disparity occurs near the pressure wall.

A direct comparison is made between the model expressions of the same components of Reynolds stress and pressure-strain tensors to find correlations between the two at the various rotation rates. In figures 4.1 - 4.3, it is observed that for all rotational rates, Π_{11} is a loss term in relation to $\overline{u'u'}$, and Π_{22} and Π_{33} are gain terms relative to their corresponding Reynolds normal stresses. This is expected because the main contribution of the pressure-strain correlation term is to isotropize (return-to-isotropy) the energy balance between the Reynolds stresses. In turbulent channel flow, the production term contributes heavily to $\overline{u'u'}$, but not $\overline{v'v'}$ and $\overline{w'w'}$, resulting in non-isotropy. Consequently, the pressure-strain isotropizes the Reynolds stresses through a negative contribution to $\overline{u'u'}$ and positive contributions to $\overline{v'v'}$ and $\overline{w'w'}$.

The modeled pressure-strain values are highly over-estimated near the channel walls in the non-rotating case (A), although this disparity decreases as the rotation rate increases near the suction wall. It is also seen that these over-approximations have a significant effect on the modeled amplitudes of the corresponding Reynolds stresses near the channel walls. The corresponding modeled Reynolds stress amplitudes near the channel walls are smaller than those of the DNS distribution for $\overline{u'u'}$, but larger than those of the DNS distributions in the cases of $\overline{v'v'}$ and $\overline{w'w'}$. Due to the amplitudes near the channel walls being significantly larger than those of the DNS data for the modeled pressure-strain tensor components Π_{11}, Π_{22} and Π_{33}, these results are expected as Π_{11} removes energy from $\overline{u'u'}$ while Π_{22} and Π_{33} contribute energy to $\overline{v'v'}$ and $\overline{w'w'}$, respectively. At the highest rotation rate, there is less effect of the modeled pressure-strain errors on the modeled Reynolds stresses. Also, the most accurate distribution of the pressure-strain for both the SG and Girimaji models relative to the DNS occurred for Π_{33} at $Ro_m = 0.5$, which corresponded with the most accurate distribution of the Reynolds stresses, $\overline{w'w'}$, for both models. As model inaccuracies of the pressure-strain in both the SG and Girimaji models have been shown to correlate with errors in the modeled Reynolds stresses, future study will involve an adjustment to both EARSM-type models in regards to their application of the SSG pressure-strain function. With the focus on improvement of pressure-strain modeling within these models such as the incorporation of an end-wall function to the SSG function so the modeled pressure strain exhibits accurate values especially near the channel walls, further research contains the potential to resolve the modeled Reynolds stress inaccuracies for both explicit algebraic Reynolds stress models near the channel walls for rotating turbulent channel flow.

Chapter 5

Conclusion

The goal of this work was to examine the turbulence statistics from a direct numerical simulation of spanwise-rotating turbulent channel flow and compare the accuracy of three commonly-used RANS-based turbulence models. Three cases of direct numerical simulations were run until a quasi-periodic steady-state was reached for rotation numbers $Ro_c = 0$, 5.2, and 26. These results were compared to similar DNS studies and subsequently validated. It was demonstrated that the EARSM-type Speziale-Gatski (SG) model was generally the most accurate in modeling Reynolds stress distributions across the channel relative to the DNS data. The modeled pressure-strain distributions of the EARSM-type SG and Girimaji models were compared directly to the values extracted from the DNS, and it was demonstrated that the accuracy of the modeled pressure-strain tensor components had a significant influence on the accuracy of the corresponding modeled distributions of the Reynolds stress tensor at all rotation numbers. A proposed correction was provided to remove a discontinuity in the Girimaji-modeled Reynolds shear stress in the non-rotational case.

Bibliography

S. Achrya, E. Sethuraman, and S. Nikotopoulos. Mass and heat transfer in rotating, smooth, high aspect ratio coolant channels with curved walls. J. Turbomachinery, 131:1–8, 2012.

S. Girimaji. Fully explicit and self-consistent reynolds stress model. Theo. Comp. Fluid Mech., 8: 387–402, 1996.

O. Grundestam, S. Wallin, and A. Johansson. Direct numerical simulations of rotating turbulent channel flow. J. Fluid Mech., 598:177–199, 2008.

K. Hanjalic and B. Launder. Contribution towards a reynolds stress closure for low reynolds number turbulence. J. Fluid Mech., 74:593–610, 1976.

J. Johnston, R. Halleen, and D. Lezius. Effects of spanwise rotation on the structure of two dimensional fully developed turbulent channel flow. J. Fluid Mech., 56:533–559, 1972.

J. Kim, P. Moin, and R. Moser. Turbulence statistics in fully developed channel flow at low reynolds number. J. Fluid Mech., 177:133–166, 1987.

R. Kristofferson and H. Andersson. Direct simulations of low reynolds number turbulent flow in a rotating channel. J. Fluid Mech., 253:163–197, 1993.

A. Kucala and S. Biringen. Spatial simulation of channel flow instability and control. J. Fluid Mech., in press.

B. Launder, G. Reece, and W. Rodi. Progress in the development of a reynolds stress turbulent closure. J. Fluid Mech., 68:537–566, 1975.

N. Liu and X. Lun. Direct numerical simulation of spanwise rotating turbulent channel flow with heat transfer. Int. J. Num. Meth. Fluids, 53:1689–1706, 2007.

J. Lumley. Toward a turbulent constitutive relation. J. Fluid Mech., 41:413–434, 1970.

S. Marlatt and S. Biringen. Numerical simulation of spatially evolving Ekman layer instability. Phys. Fluids, 7:449–451, 1995.

S. Marlatt, S. Waggy, and S. Biringen. Direct Numerical Simulation of the Turbulent Ekman Layer: Turbulent Energy Budgets. J. Thermophysics Heat Transfer, 24:544–555, 2010.

S. Marlatt, S. Waggy, and S. Biringen. Direct Numerical Simulation of the Turbulent Ekman Layer: Evaluation of Closure Models. J. Atm. Sci., 69:1106–1117, 2012.

S. W. Marlatt. Direct Numerical Simulation of Ekman Layer Transition and Turbulence. PhD thesis, University of Colorado, Boulder, 1994.

P. Moin and J. Kim. Numerical investigation of turbulent channel flow. J. Fluid Mech., 118:341–377, 1982.

Y. Nagano and H. Hattori. Direct numerical simulation and modeling of spanwise rotating channel flow with heat transfer. J. Turbulence, 4:1–15, 2003.

S. Pope. A more general effective eddy viscosity hypothesis. J. Fluid Mech., 72:331–357, 1975.

B. P. Reif, P. Durbin, and A. Ooi. Modeling rotational effects in eddy-viscosity closure. Int. J. Heat Fluid Flow, 20:563–573, 1999.

W. Reynolds. Computation of turbulent flows. Ann. Rev. Fluid Mech., 8:183–208, 1976.

U. Schumann. Realizability of Reynolds-stress turbulence models. Phys. Fluids, 20:721–725, 1977.

C. Speziale and T. Gatski. On Explicit Algebraic Stress Models for Complex Turbulent Flows. J. Fluid Mech., 254:59–78, 1993.

C. Speziale, S. Sarkar, and T. Gatski. Modeling the Pressure-strain correlation of Turbulence: An Invariant Dynamical System Approach. J. Fluid Mech., 227:245–272, 1991.

S. Waggy. Turbulent Transport in the Atmospheric Boundary Layer with Application to Wind Farm Dynamics. PhD thesis, University of Colorado, Boulder, 2009.

S. Waggy, S. Biringen, and P. Sullivan. Direct numerical simulation of top-down and bottom-up diffusion in the convective boundary layer. J. Fluid Mech., 724:581–606, 2013.

H. Wu and N. Kasagi. Effects of arbitrary directional system rotation on turbulent channel flow. Phys. Fluids, 16:979–990, 2004.

Appendix A

Derivation of the $\overline{v^2} - f$ model

These equations cover the basis of the $\overline{v^2} - f$ model's formulation of its expression for the modeled Reynolds stresses. For the original source material of the $\overline{v^2} - f$ model, readers are referred to Reif et al. (1999). Given in Pope (1975), the most general representation function for the Reynolds stresses is written as

$$\frac{\overline{u_i' u_j'}}{k} = \frac{2}{3}\delta_{ij} - aS_{ij} - b(S_{ij}W_{kj} - W_{ik}S_{kj}) - c(S_{ij}^2 - \frac{1}{3}S^2\delta_{ij}) \tag{A.1}$$

with the coefficients a, b and c, being functions of the invariants of the mean strain-rate tensor (S^2 or η_1), rotation tensor (W^2 or η_2), and scalar properties of the turbulence field. Unlike explicit algebraic Reynolds stress models, the $\overline{v^2} - f$ model only retains terms up for the first order and consequently applies the equation

$$\frac{\overline{u_i' u_j'}}{k} = \frac{2}{3}\delta_{ij} - 2C_\mu^* \frac{\overline{v^2}}{k} T S_{ij} \tag{A.2}$$

with the scalars k and $\overline{v^2}$ being taken from the set of four transport equations that are shown in A.3 - A.6.

$$\frac{Dk}{Dt} = P - \varepsilon + \frac{\partial}{\partial x_j}((\nu + \nu_t)\frac{\partial k}{\partial x_j}) \tag{A.3}$$

$$\frac{D\varepsilon}{Dt} = \frac{C_{\epsilon 1}^* P - C_{\epsilon 2}\varepsilon}{T} + \frac{\partial}{\partial x_j}((\nu + \frac{\nu_t}{\sigma_\epsilon})\frac{\partial \varepsilon}{\partial x_j}) \tag{A.4}$$

$$\frac{D\overline{v^2}}{Dt} = kf - \frac{\overline{v^2}}{k} + \frac{\partial}{\partial x_j}((\nu + \nu_t)\frac{\partial \overline{v^2}}{\partial x_j}) \tag{A.5}$$

$$f - L^2\nabla^2 f = (C_1 - 1)\frac{2/3 - \overline{v^2}/k}{k} + C_2\frac{P}{k} \tag{A.6}$$

where

$$\nu_t = C_\mu \overline{v^2} T, \quad P = 2\nu_t S^2 \tag{A.7}$$

and

$$L = C_L \frac{k^{3/2}}{\varepsilon}, \quad T = \frac{k}{\varepsilon} \tag{A.8}$$

The model coefficients are shown in table 3.1 and for numerical computations, the solid wall boundary conditions are

$$U_i = 0, \ \overline{v^2} = 0, \ k = 0, \ f_{wall} = lim_{d\to 0}[\frac{-20\nu^2\overline{v^2}}{\varepsilon d^4}] \tag{A.9}$$

As this model considers rotational effects, these influences must be considered within the eddy viscosity coefficient. The mean strain-rate tensor is frame-indifferent, and consequently the effects of rotation are shown in the definition of the rotation tensor in the $\overline{v^2} - f$ model:

$$W_{ik} = \frac{1}{2} T[(\frac{\partial U_i}{\partial x_k} - \frac{\partial U_k}{\partial x_i}) + 2C_w \epsilon_{kim} \Omega_m] \tag{A.10}$$

where C_w is a model-dependent coefficient with a value of 2.25 in the $\overline{v^2} - f$ model. In order to derive the final unknown coefficient in the turbulence model, C_μ^*, Reif et al. (1999) derives two more evolution equations featuring the terms $\overline{v^2}/k$ and timescale ratio ϵ/Sk, where S is the principal rate-of-strain. New invariants are derived from these equations and an equilibrium range of invariant values is established where both the timescale and production-dissipation ratios are stable. These correlations assert a relationship between the two invariants of the strain-rate and rotation tensors and the C_μ^* coefficient. For adequate model consideration in complex non-equilibrium flows, a third invariant is introduced into the model, η_3, being the absolute value of the difference between the first two invariants. A heavy derivation is then conducted that focuses on model bifurcation and the forcing of variables to adhere to stability and equilibrium constraints; eventually the final form of the modeled C_μ^* term is derived and written as

$$C_\mu^* = C_\mu \frac{1 + \alpha_2\eta_3 + \alpha_3\eta_3}{1 + \alpha_4\eta_3}((\frac{1 + \alpha_5\eta_1}{1 + \alpha_5\eta_2})^{1/2} + \alpha_1(\eta_2)^{1/2}(\eta_3 - \eta_2)^{1/2})^{-1} \tag{A.11}$$

with the model coefficients being given by $(\alpha_1, \alpha_2, \alpha_3, \alpha_4, \alpha_5) = (0.055, 0.5, 0.25, 0.2, 0.025)$.

Appendix B

Derivation of the Speziale-Gatski model

These equations cover the basis of the Speziale-Gatski (SG) model's formulation of its expression for the modeled Reynolds stresses. For a reference to the original source material of the Speziale-Gatski model, readers are referred to Speziale and Gatski (1993). As the Speziale-Gatski model is an explicit algebraic Reynolds stress model, its formulation begins with the exact Reynolds stress transport equation given by

$$\frac{\partial \overline{u_i' u_j'}}{\partial t} = P_{ij} - \epsilon_{ij} + \phi_{ij} + D_{ij} \tag{B.1}$$

where P_{ij}, ϵ_{ij}, ϕ_{ij}, and D_{ij} represent the production, dissipation, pressure-strain and diffusion terms that are functions of the Reynolds stresses or higher-order velocity correlations. Using the definition of the anisotropic tensor as a function of the Reynolds stress tensor

$$b_{ij} = \frac{\overline{u_i' u_j'}}{2k} - \frac{1}{3}\delta_{ij} \tag{B.2}$$

the Reynolds stress equation is modified into the function of the anisotropic tensor, mean strain rate tensor, rotation tensor and other flow-dependent scalars shown in equation B.3

$$(P - \epsilon) b_{ij} = -\frac{2}{3} k S_{ij} - k(b_{ij} S_{jk} + b_{jk} S_{ik} - \frac{2}{3} b_{lm} S_{lm} \delta_{ij}) - k(b_{ik} W_{jk} + b_{jk} W_{ik}) + \frac{1}{2} \Pi_{ij} \tag{B.3}$$

with Π_{ij} representing a pressure-strain representation function. The SG model uses the popular Speziale, Sarkar, and Gatski (SSG) pressure-strain function derived in Speziale et al. (1991).

The insertion of the SSG function into equation B.3 yields the following implicit relationship

for the anisotropic tensor b_{ij}:

$$b_{ij} = \frac{1}{2}g\tau[(C_2 - \frac{4}{3}S_{ij} + (C_3 - 2)(b_{ij}S_{jk} + b_{jk}S_{ik} - \frac{2}{3}b_{lm}S_{lm}\delta_{ij}) + (C_4 - 2)(b_{ik}W_{jk} + b_{jk}W_{ik}] \quad \text{(B.4)}$$

with g and τ being defined as

$$g = (\frac{C_1}{2} + \frac{P}{\epsilon} - 1)^{-1} \quad \text{(B.5)}$$

$$\tau = \frac{k}{\varepsilon} \quad \text{(B.6)}$$

Equation B.4 is then written in matrix form as shown in equation B.7, and the Speziale-Gatski model calculates the explicit solution of the anisotropic tensor in matrix form, b^*, as a function of the strain-rate (S^*) and rotation tensors (W^*) in matrix form.

$$b^* = -S^* - (b^*S^* + S^*b^* - \frac{2}{3}(b^*S^*)I) + b^*W^* - W^*b^* \quad \text{(B.7)}$$

The invokation of form invariance under an orthogonal coordinate transformation causes equation B.7 to become

$$Qf(S^*, W^*)Q^T = f(QS^*Q^T, QW^*Q^T) \quad \text{(B.8)}$$

with Q representing the rotation matrix. In order to satisfy equation B.8, the following general solution for b^* is mandatory:

$$b^* = \sum_{\lambda}^{10} G^{(\lambda)}T^{(\lambda)} \quad \text{(B.9)}$$

where $T^{(\lambda)}$ are the integrity basis for functions of a symmetric and antisymmetric tensor and $G^{(\lambda)}$ are scalar functions of the invariants S^* and W^*. Using the ten integrity basis relations for $T^{(\lambda)}$ covered in Pope (1975) and the definition of $G^{(\lambda)}$ as functions of five irreducible invariants: $S^{*2}, W^{*2}, S^{*3}, S^*W^{*2}, S^{*2}W^{*2}$, these functions are substituted into equation B.9 and solved using tensorial algebra and the application of the Cayley-Hamilton Theorem. Using the redundancies of the integrity basis, expressions are found for three unique solutions of $G^{(\lambda)}$, thus creating the following solution for the anistropic tensor in matrix form:

$$b^* = -\frac{3}{3 - 2\eta_1 - 6\eta_2}[S^* + (S^*W^* - W^*S^*) - 2(S^{*2} - \frac{1}{3}S^{*2}I)] \quad \text{(B.10)}$$

To convert this solution for the anisotropic tensor in matrix form into a general solution for the anistropic tensor, the main challenge is to regularize the algebraic stress model created thus far. The Speziale-Gatski model uses a Pade approximation, which is a well-regarded mathematical technique that approximates a given function so that the power series of the approximant is identical to that of the function that it is estimating. Using this approximation, the main coefficient in equation B.12 is then written as

$$\frac{3}{3-2\eta_1-6\eta_2} = \frac{3(1+\eta^2)}{3+\eta^2+6\eta^2\zeta^2+6\zeta^2} \tag{B.11}$$

with the invariants being $\eta = (S_{ij}S_{ij})^{1/2}$ and $\zeta = (W_{ij}W_{ij})^{1/2}$. The regularized model for the anistropic tensor is consequently

$$b^* = -\frac{3(1+\eta^2)}{3+\eta^2+6\eta^2\zeta^2+6\zeta^2}[S^* + (S^*W^* - W^*S^*) - 2(S^{*2} - \frac{1}{3}S^{*2}I)] \tag{B.12}$$

By using equation B.2, equation B.12 is easily converted into a modeled expression for the Reynolds stresses, thus completing the Speziale-Gatski model.

Appendix C

Derivation of the Girimaji model

These equations cover the basis of the Girimaji turbulence model's formulation for its expression of the modeled Reynolds stresses. For a reference to the original source material of the Girimaji model, readers are referred to Girimaji (1996). The main derivations of the Girimaji turbulence model are centered about the anisotropic tensor rather than the Reynolds stress tensor, but the two tensors are related easily using the following expression:

$$b_{ij} = \frac{\overline{u_i' u_j'}}{2k} - \frac{1}{3}\delta_{ij} \tag{C.1}$$

As the Girimaji model is a nonlinear eddy viscosity model, the turbulence model approximates the Reynolds stresses as a nonlinear representation function that is a function of the mean strain-rate tensor, rotation tensor, and production-dissipation ratio. This representation function is then substituted into the exact Reynolds stress transport equation given by

$$\frac{\partial \overline{u_i' u_j'}}{\partial t} = P_{ij} - \epsilon_{ij} + \phi_{ij} + D_{ij} \tag{C.2}$$

where P_{ij}, ϵ_{ij}, ϕ_{ij}, and D_{ij} represent the production, dissipation, pressure-strain and diffusion terms that are functions of the Reynolds stresses or higher-order velocity correlations. By transforming the Reynolds stress equation into a partial differential equation for the anisotropic tensor and invoking the 'weak equilibrium' assumption that presumes a constant ratio between the production and dissipation, the Girimaji model creates the following nonlinear algebraic Reynolds stress equation

$$b_{ij}[L_{01} - L_{11} b_{mn} S_{mn}] = L_2 S_{ij} L_3 (b_{ij} S_{jk} + b_{jk} S_{ik} - \frac{2}{3} b_{lm} S_{lm} \delta_{ij}) + L_4 (b_{ik} W_{jk} + b_{jk} W_{ik}) \tag{C.3}$$

where the L coefficients are shown in table 3.3. Once the nonlinear algebraic Reynolds stress equation has been constructed, the Girimaji model uses the most general nonlinear representation function of the anisotropic tensor shown in equation C.4 and solves for the unknown coefficients $G_1 - G_3$.

$$b_{ij} = G_1 S_{ij} + G_2(S_{ik}W_{kj} + W_{ik}S_{kj}) + G_3(S_{ik}S_{kj} - \frac{1}{3}S_{mn}S_{mn}\delta_{ij}) \tag{C.4}$$

By substituting the relation

$$b_{mn}S_{mn} = G_1\eta_1 \tag{C.5}$$

and equation C.4 into equation C.3, the following implicit relationship for the G coefficients is derived after several manipulations:

$$\begin{aligned} &G_1 S_{ij} + G_2(S_{ik}W_{kj} + W_{ik}S_{kj}) + G_3(S_{ik}S_{kj} - \frac{1}{3}S_{mn}S_{mn})(L_{01} - \eta_1 L_{11}G_1) \\ &= [L_2 + \frac{\eta_1}{3}L_3G_3 + 2\eta_2 L_4 G_2]S_{ij} + 2L_3G_1(S_{ik}S_{kj} - \frac{1}{3}S_{mn}S_{mn}\delta_{ij}) - L_4G_1(S_{ik}W_{kj} + W_{ik}S_{kj}) \end{aligned} \tag{C.6}$$

A constraint is extracted from equation C.6 by comparing the coefficients of the mean strain-rate tensor S_{ij} as shown in equation C.7, and the coefficients of the parenthesized terms lead to the following definitions of G_2 and G_3 as a function of G_1 in equation C.8.

$$G_1(L_{01} - \eta_1 L_{11}G_1) = L_2 + \frac{\eta_1}{3}L_3G_3 + 2\eta_2 L_4 G_2 \tag{C.7}$$

$$\begin{aligned} G_2 &= -\frac{L_4G_1}{L_{01}^2 - \eta_1 L_{11}G_1} \\ G_3 &= -\frac{L_4G_1}{L_{01}^2 - \frac{2}{3}\eta_2 L_3 + \eta_1 L_{11}G_1} \end{aligned} \tag{C.8}$$

As the last problem is to compute the final unknown coefficient G_1, a cubic equation for G_1 is derived by substituting the definitions of G_2 and G_3 in equation C.8 into equation C.7:

$$(\eta_1 L_{11})^2 G_1^3 - (2\eta_1 L_{01} L_{11})G_1^2 + [(L_{01})^2 + \eta_1 L_{11}L_2 - \frac{2}{3}\eta_1(L_3)^2 + 2\eta_2(L_4)^2]G_1 - L_{01}L_2 = 0 \tag{C.9}$$

The Girimaji then undertakes a complex mathematical derivation as the calculation of G_1 is difficult and the cubic equation produces multiple real roots; a correct choice of G_1 among the possible roots is necessary for an applicable turbulence model. The following variable definitions

in equation C.10 are used in the solution of the cubic equation.

$$\begin{aligned}
\cos(\theta) &= -1 \\
p &= -\frac{2L_{01}}{\eta_1 L_{11}} \\
r &= -\frac{L_{01}L_2}{(\eta_1 L_{11})^2} \\
a &= q - \frac{p^2}{3} \\
q &= \frac{1}{(\eta_1 L_{11})^2}[L_{01}^2 + \eta_1 L_{11} L_2 - \frac{2}{3}\eta_1 L_3^2 + 2\eta_2 L_4^2] \\
b &= \frac{1}{27}(2p^3 - 9pq + 27r) \\
D &= \frac{b^2}{4} + \frac{a^3}{27}
\end{aligned} \tag{C.10}$$

For two conditions, when $\eta_1 = 0$ and $L_{01} = 0$, equation C.9 decomposes into a linear equation so the definition of G_1 is straight-forward to calculate. For the other conditions, a complex root analyses and selection criterion takes place, and the final expression for G_1 in all cases is shown in equation C.11, consequently completing the Girimaji turbulence model's formulation and derivation.

$$G_1 = \begin{cases}
\frac{L_{01}L_2}{L_{01}^2 + 2\eta_2 L_4^2} & \text{when } \eta_1 = 0 \\
-\frac{p}{3} + (-\frac{b}{2} + \sqrt{D})^{1/3} + (-\frac{b}{2} - \sqrt{D})^{1/3} & \text{when } D > 0 \\
-\frac{p}{3} + 2\sqrt{-\frac{a}{3}}\cos(\frac{\theta}{3}) & \text{when } D < 0 \text{ and } b < 0 \\
-\frac{p}{3} + 2\sqrt{-\frac{a}{3}}\cos(\frac{\theta}{3} + \frac{2\pi}{3}) & \text{when } D < 0 \text{ and } b > 0
\end{cases} \tag{C.11}$$

Appendix D

Intercomponent energy transfer in the Reynolds stress equation

The Reynolds stress equation is derived from the notion of averaging the quantities within the incompressible Navier-Stokes equations, shown in equations D.1 and D.2 into an average component (U_i) and a fluctuating component (u_i).

$$\frac{\partial u_i}{\partial x_i} = 0 \tag{D.1}$$

$$\frac{\partial u_i}{\partial t} + u_k \frac{\partial u_i}{\partial x_k} = -\frac{1}{\rho}\frac{\partial p}{\partial x_i} + \nu \frac{\partial^2 u_i}{\partial x_l \partial x_l} \tag{D.2}$$

When averaging is applied to the conservation of momentum equation, the new evolution equation for the velocity becomes

$$\frac{\partial u_i}{\partial t} + U_k \frac{\partial U_i}{\partial x_k} + u_k \frac{\partial U_i}{\partial x_k} + U_k \frac{\partial u_i}{\partial x_k} + \frac{\partial}{\partial x_k}(u_i u_k) = -\frac{1}{\rho}\frac{\partial P}{\partial x_i} - \frac{1}{\rho}\frac{\partial p}{\partial x_i} + \nu \frac{\partial^2}{\partial x_l \partial x_l}(U_i + u_i) \tag{D.3}$$

When this equation subtracts its average value, the new expression shown in equation D.4 is obtained which includes new terms known as the Reynolds stresses ($\overline{u_i u_k}$); equation D.4 is also known as the Reynolds-Averaged Navier-Stokes (RANS) equation.

$$\frac{\partial u_i}{\partial t} + u_k \frac{\partial U_i}{\partial x_k} + U_k \frac{\partial u_i}{\partial x_k} + \frac{\partial}{\partial x_k}(u_i u_k - \overline{u_i u_k}) = -\frac{1}{\rho}\frac{\partial p}{\partial x_i} + \nu \frac{\partial^2 u_i}{\partial x_l \partial x_l} \tag{D.4}$$

The Reynolds stress equation is derived from the RANS equation by first multiplying equation D.4 by the velocity component u_j. When the same RANS equation is written for velocity component u_j and multipled by u_i, these two equations are added and averaged to form the Reynolds

stress equation shown in equation D.5.

$$\begin{aligned}&\frac{\partial\overline{u_iu_j}}{\partial t}+\overline{u_ju_k}\frac{\partial U_i}{\partial x_k}+\overline{u_iu_k}\frac{\partial U_j}{\partial x_k}+U_k\frac{\partial\overline{u_iu_j}}{\partial x_k}\\&=-\overline{(u_j\frac{\partial}{\partial x_k}u_iu_k}+\overline{u_i\frac{\partial}{\partial x_k}u_ju_k})-\frac{1}{\rho}\overline{(u_j\frac{\partial p}{\partial x_i}}+\overline{u_i\frac{\partial p}{\partial x_j}})+\nu\overline{(u_j\frac{\partial^2u_i}{\partial x_l\partial x_l}}+\overline{u_i\frac{\partial^2u_j}{\partial x_l\partial x_l}})\end{aligned}\tag{D.5}$$

Further manipulation of equation D.5 produces an alternative form of the Reynolds stress equation:

$$\begin{aligned}&\frac{\partial\overline{u_iu_j}}{\partial t}+\overline{u_ju_k}\frac{\partial U_i}{\partial x_k}+\overline{u_iu_k}\frac{\partial U_j}{\partial x_k}+U_k\frac{\partial\overline{u_iu_j}}{\partial x_k}\\&=-\frac{\partial}{\partial x_k}\overline{u_iu_ju_k}-\frac{1}{\rho}(\frac{\partial}{\partial x_i}\overline{pu_j}+\frac{\partial}{\partial x_j}\overline{pu_i})+\frac{1}{\rho}\overline{p(\frac{\partial u_j}{\partial x_i}+\frac{\partial u_j}{\partial x_i})}+\nu\frac{\partial^2\overline{u_iu_j}}{\partial x_l\partial x_l}+2\nu\overline{\frac{\partial u_i}{\partial x_l}\frac{\partial u_j}{\partial x_l}}\end{aligned}\tag{D.6}$$

An examination of the non-zero components yields important information about the inter-component energy transfer for the various correlation tensors, and hence the equations for $\overline{u_1^2}$, $\overline{u_2^2}$, $\overline{u_3^2}$ and $\overline{u_1u_2}$ are

$$\frac{\partial\overline{u_1^2}}{\partial t}=-2\overline{u_1u_2}\frac{\partial U_1}{\partial x_2}-\frac{\partial}{\partial x_2}\overline{u_1^2u_2}+\frac{2}{\rho}\overline{p\frac{\partial u_1}{\partial x_1}}+\nu\frac{\partial^2\overline{u_1^2}}{\partial x_2^2}-2\nu\overline{\frac{\partial u_1}{\partial x_l}\frac{\partial u_1}{\partial x_l}}\tag{D.7}$$

$$\frac{\partial\overline{u_2^2}}{\partial t}=-\frac{\partial}{\partial x_2}\overline{u_2^3}-\frac{2}{\rho}\frac{\partial}{\partial x_2}\overline{pu_2}+\frac{2}{\rho}\overline{p\frac{\partial u_2}{\partial x_2}}+\nu\frac{\partial^2\overline{u_2^2}}{\partial x_2^2}-2\nu\overline{\frac{\partial u_2}{\partial x_l}\frac{\partial u_2}{\partial x_l}}\tag{D.8}$$

$$\frac{\partial\overline{u_3^2}}{\partial t}=-\frac{\partial}{\partial x_2}\overline{u_3^2u_2}+\frac{2}{\rho}\overline{p\frac{\partial u_3}{\partial x_3}}+\nu\frac{\partial^2\overline{u_3^2}}{\partial x_2^2}-2\nu\overline{\frac{\partial u_3}{\partial x_l}\frac{\partial u_3}{\partial x_l}}\tag{D.9}$$

$$\frac{\partial\overline{u_1u_2}}{\partial t}=-\overline{u_2^2}\frac{\partial U_1}{\partial x_2}-\frac{\partial}{\partial x_2}\overline{u_1(u_2^2+\frac{p}{\rho})}+\overline{\frac{p}{\rho}(\frac{\partial u_2}{\partial x_1}+\frac{\partial u_1}{\partial x_2})}+\nu\frac{\partial^2\overline{u_1u_2}}{\partial x_2^2}-2\nu\overline{\frac{\partial u_1}{\partial x_l}\frac{\partial u_2}{\partial x_l}}\tag{D.10}$$

Therefore, the temporal changes to $\overline{u_1^2}$, $\overline{u_2^2}$, $\overline{u_3^2}$ and $\overline{u_1u_2}$ are determined by convective diffusion and viscous effects due to several factors: flow field inhomogeneities in the x_2-direction, production of stresses, correlations between the pressure fluctuations and mean velocity gradients (also known as pressure-strain correlations) and by dissipative viscous effects.

For the normal Reynolds stresses, it is noted that the production term is only present in the evolution equation for $\overline{u_1^2}$. From equation D.10, if the mean velocity gradient $\frac{\partial U_1}{\partial x_2}$ is positive, then the corresponding Reynolds stress term $\overline{u_2^1}$ is negative, causing the production term in equation D.7 to have a positive contribution to the temporal changes in $\overline{u_1^2}$. As the production term is not

present in the equations for the other normal Reynolds stress components, the production of turbulence results in non-isotropy. The viscous terms on the other hand are present in the evolution equations of all four components and these terms universally make a negative contribution to the turbulence intensity.

An examination of the pressure-velocity-gradient correlation, also known as the pressure-strain correlation, proceeds with the assumption that the pressure-strain correlation term $\overline{p\partial u_1/\partial x_1}$ makes a negative contribution to the temporal changes of $\overline{u_1^2}$ if $\overline{u_1^2}$ is much larger than $\overline{u_2^2}$ and $\overline{u_3^2}$. The resulting spatial deccelerating inward of velocity component u_1 is associated with a positive value of local pressure p, so the pressure-strain component $\overline{p\partial u_1/\partial x_1} \leq 0$; but the other pressure strain components $\overline{p\partial u_2/\partial x_2}$ and $\overline{p\partial u_3/\partial x_3}$ subsequently must be positive to satisfy continuity. If the opposite case of a spatial accelerating outward velocity component u_1 is considered, the pressure-strain terms continue to maintain their respective positive and negative contributions, thus these results are extrapolated to on the average.

Once these contributions are factored into the temporal evolution equations, it is seen that the pressure-strain term carries a negative contribution for the large u_1 turbulent velocity, but a positive contribution for the small u_2 and u_3 velocities. The effect of the pressure-strain correlation term is ostensibly then to make the three turbulence velocity components equal, and the term acts as a 'return-to-isotropy' term. Consequently, it is reasonable to assume that the transfer of energy from the higher-intensity component to the lower-intensity components is proportional to the differences in intensity between the correlations.

For the shear Reynolds stress $\overline{u_1u_2}$, equation D.10 is examined to analyze the various budget term contributions. For the case of $\frac{\partial U_1}{\partial x_2} \geq 0$, the production term makes a negative contribution to the shear Reynolds stress. But because the assumption $\frac{\partial U_1}{\partial x_2} \geq 0$ implies that $\overline{u_1u_2}$ is negative, the negative contribution actually causes an increase in the amplitude of $\overline{u_1u_2}$. The opposite contribution is observed for the converse case.

To examine the contribution from the pressure-strain correlation term

$$\overline{\frac{p}{\rho}(\frac{\partial u_2}{\partial x_1}+\frac{\partial u_1}{\partial x_2})} \tag{D.11}$$

in the evolution equation for $\overline{u_1 u_2}$, the correlation $\overline{u_1 u_2}$ is written in terms of turbulent velocity components u_1^* and u_2^* aligned in a pair of new axes that are at an angle of 45 degrees to the original axes, so that the new axes become the principal axes in the turbulence-stress distribution.

$$2\overline{u_1 u_2} = \overline{u_1^{*2}} - \overline{u_2^{*2}} \tag{D.12}$$

The following relation is then derived for the pressure-strain correlation term as a function of the the new velocities by applying the same transformation of the coordinate axes to the velocity gradients:

$$\overline{p(\frac{\partial u_2}{\partial x_1}+\frac{\partial u_2}{\partial x_1})} = \overline{p(\frac{\partial u_2^*}{\partial x_1^*}-\frac{\partial u_2^*}{\partial x_1^*})} \tag{D.13}$$

Assuming the proportional energy transfer relation from the previous section and the relation in equation D.12, the following equation is obtained between the pressure-strain correlation term and the shear Reynolds stress:

$$\overline{p(\frac{\partial u_2}{\partial x_1}+\frac{\partial u_2}{\partial x_1})} \sim -4\overline{u_1 u_2} \tag{D.14}$$

The pressure-strain term and $\overline{u_1 u_2}$ will always have opposite signs. Subsequently, it is seen that the effect of the pressure-strain term is to decrease the absolute value of the shear Reynolds stress term.